

Extrplanar emission in isolated edge-on late-type galaxies.

I. The H α distribution versus to the old and young stellar discs.★

Minerva M. Sardaneta,¹† Philippe Amram,² Roberto Rampazzo,³ Margarita Rosado,¹ Mónica Sánchez-Cruces,¹ Isaura Fuentes-Carrera⁴ and Soumavo Ghosh⁵

¹Universidad Nacional Autónoma de México. Instituto de Astronomía. A.P. 70-264, 04510. Ciudad de México, México

²Aix Marseille Univ, CNRS, CNES, LAM, Marseille, France

³INAF-Osservatorio Astrofisico di Asiago, Via dell'Osservatorio 8, 36012 Asiago, Italy

⁴Escuela Superior de Física y Matemáticas, Instituto Politécnico Nacional, U.P. Adolfo López Mateos, C.P.07738, Ciudad de México, México

⁵Max-Planck-Institut für Astronomie, Königstuhl 17, D-69117 Heidelberg, Germany

Accepted XXX. Received YYY; in original form ZZZ

ABSTRACT

Isolated galaxies are the ideal reference sample to study the galaxy structure minimising potential environmental effects. We selected a complete sample of 14 nearby, late-type, highly inclined ($i \geq 80^\circ$), isolated galaxies from the Catalogue of Isolated Galaxies (CIG) which offers a vertical view of their disc structure. We aim to study extrplanar Diffuse Ionized Gas (eDIG) by comparing the old and young disc components traced by near-infrared (*NIR*) and Ultraviolet (*UV*) imaging with the H α emission structure. We obtained H α monochromatic maps from the Fabry-Perot (FP) interferometry, while the old and young discs structures are obtained from the photometric analysis of the 2MASS K_s -band, and GALEX *NUV* and *FUV* images, thereby identifying the stellar disc and whether the eDIG is present. The H α morphology is peculiar in CIG 71, CIG 183, CIG 593 showing clear asymmetries. In general, geometric parameters (isophotal position angle, peak light distribution, inclination) measured from H α , *UV* and *NIR* show minimal differences (e.g. $\Delta i \leq \pm 10^\circ$), suggesting that interaction does not play a significant role in shaping the morphology, as expected in isolated galaxies. From H α maps, the eDIG was detected vertically in 11 out of 14 galaxies. Although the fraction of eDIG is high, the comparison between our sample and a generic sample of inclined spirals suggests that the phenomenon is uncorrelated to the galaxy environment. As suggested by the extrplanar *UV* emission found in 13 out of 14 galaxies the star formation extends well beyond the disc defined by the H α map.

Key words: galaxies: haloes – galaxies: evolution – galaxies: ISM – galaxies: photometry – galaxies: stellar content – galaxies: fundamental parameters

1 INTRODUCTION

Galaxy interactions dramatically impact several galaxy properties, such as their morphology and star-formation history (see e.g. Rampazzo et al. 2016, and references therein). The idea of gathering catalogues of isolated galaxies has been developed at least since the 1970s (e.g. the *Catalogue of Isolated Galaxies* (CIG), Karachentseva 1973) as a baseline for comparison with galaxies located in denser environments subject to interaction-induced phenomena. In the last decades, catalogues of isolated galaxies, selected from very low galaxy density regions, have been either implemented or revised using redshift measurements (Verdes-Montenegro et al. 2005; Karachentseva et al. 2010; Argudo-Fernández et al. 2013, 2015). A recent H I study of isolated galaxy samples suggests a picture of "nurture free" galaxies (Jones et al. 2018). Other works (see e.g. Rampazzo et al. 2020) have shown that isolated elliptical galaxies suffered past interactions from which they still show the

'scars', although they have probably not experienced gravitational influences from their close neighbours over the past billion years.

This paper concentrates on the stellar versus H α components in isolated spiral galaxies seen nearly edge-on ($i \geq 80^\circ$). This galactic configuration relative to the sky plane provides more information on the vertical structure of the disc (e.g. Burstein 1979; Fraternali & Binney 2006; Kamphuis et al. 2007; Peters et al. 2017) revealing the extrplanar Diffuse Ionized Gas (eDIG), detected in galaxies with relatively high star formation rate (SFR) surface densities (Rossa & Dettmar 2003a,b). The eDIG is usually traced at optical wavelengths using the H α recombination line (e.g. Rosado et al. 2013). In addition, as the eDIG might be spatially correlated with the star formation (SF)-gas relations, it has been observed to trace regions of H I dominance within galactic discs, especially those located outside active star-forming regions, making the 21-cm emission line a helpful tool for the eDIG detection (e.g. Zschaechner et al. 2015). Ultraviolet (*UV*) imaging can also detect the low-intensity outer star formation disc by detecting OB stars located in very low SFR density regions (e.g. Hoopes et al. 2001; Thilker et al. 2002; Gil de Paz et al. 2005; Thilker et al. 2005, 2007; Gil de Paz et al. 2007b). From the comparison between the H α and the *UV* images of spiral galaxies

★ Based on observations obtained at the Observatoire de Haute Provence (OHP, France), operated by the French CNRS.

† E-mail: mminerva@astro.unam.mx

with low inclination ($i \leq 80^\circ$), Thilker et al. (2007) showed that the Near Ultraviolet (*NUV*) emitting component is radially more extended than the emission of the old stellar population in at least 30% of galaxies from the Local Universe ($z \approx 0.02$). In high inclined galaxies, in cases where an eDIG layer does exist, the *UV* haloes tend to form a thick disc having a similar morphology to the *UV* halo and occurring in about the same place (Hodges-Kluck et al. 2016). Moreover, it has been observed that the $H\alpha$ -*UV* flux ratio is lower in the eDIG than in $H\text{II}$ regions, indicating that the field OB stars, which are situated outside the star-forming regions, are important contributors to the eDIG ionization in most of the galaxies, and even in some galaxies they may be the dominant ionization source (Hoopes et al. 2001; Hodges-Kluck et al. 2016; Jo et al. 2018).

The eDIG morphology shows a wide variety of local morphological features (Rand 1998; Rossa & Dettmar 2003b; Rosado et al. 2013) such as prominent layers of diffuse gas, filamentary structures, or just one or a few patches of extraplanar emission (Rand 1998; Rossa & Dettmar 2003b; Rosado et al. 2013). Some eDIG originating phenomena have been proposed, such as Inter Stellar Medium (ISM) activity in the galaxy disc (e.g. Heald et al. 2006a,b, 2007; Rosado et al. 2013; Ho et al. 2016; Jones et al. 2017; Bizyaev et al. 2017), intergalactic medium accretion (e.g. Putman et al. 2012; Putman 2017; Levy et al. 2019; Bizyaev et al. 2022), satellite galaxies interaction (e.g. Walker et al. 1996; Zschaechner et al. 2015) and accretion or intra-cluster interaction (e.g. Tomičić et al. 2021; Sardaneta et al. 2022; Boselli et al. 2022). In parallel, several studies have demonstrated that the *UV* halo emission is consistent with a reflection nebula produced by dust in the halo (e.g. Hodges-Kluck & Bregman 2014; Shinn & Seon 2015; Hodges-Kluck et al. 2016; Jo et al. 2018; Shinn 2019). Various mechanisms have been suggested as potential sources for diffuse-and-global *UV* haloes, including galactic radiation, magneto-hydrodynamic phenomena, and dust accretion from the circumgalactic or intergalactic medium (see Shinn & Seon 2015, for a comprehensive examination). The contribution of each process over cosmic time is still unclear as they both produce hot and cold components that occupy roughly the same space (e.g. Hodges-Kluck & Bregman 2014).

Several studies from large surveys such as SAMI¹ (Ho et al. 2016), MaNGA² (Jones et al. 2017; Bizyaev et al. 2017, 2022) and CALIFA³ (Levy et al. 2019), and from specific surveys as CHANG-ES⁴ (Lu et al. 2023) have employed various environmental definitions in the selection of their samples of edge-on galaxies, contributing to varying interpretations of the relationship between extraplanar gas properties and their host galaxies. For instance, they have either discarded major mergers with clear tidal features (Ho et al. 2016; Bizyaev et al. 2022), rejected galaxies that have another object in the field, including stars (Bizyaev et al. 2017) or excluded galaxies with distorted discs in their $H\alpha$ images (Lu et al. 2023). Recently, two studies agreed that the eDIG could be a consequence of the accretion of the CircumGalactic Medium (CGM) (Levy et al. 2019; Bizyaev et al. 2022) which has also been proposed as probable *UV* halo origin (e.g. Hodges-Kluck & Bregman 2014; Shinn & Seon 2015). However, most of the literature still lacks a general agreement on the sources of ionization for eDIG. Since the eDIG may be related to the CGM, Bizyaev et al. (2022) visually examined the outer regions of each galaxy of their sample aiming to locate environmental structures that might be connected

to the eDIG. Their findings ranged from small satellites lacking noticeable structure to large satellites even larger than the primary object. Therefore, the consensus or discrepancy in explaining the eDIG origin is likely a consequence of the different definitions of environment adopted. As a reference study case, isolated star-forming galaxies with the possibility of edge-on observations is needed.

In order to study the environmental effects on the eDIG distribution, we selected a sample of isolated nearby late-type, high-inclined galaxies from the CIG catalogue (Karachentseva 1973). Indeed, nearby galaxies are better resolved, late-type galaxies are those which contain the most $H\alpha$ emission, and almost edge-on galaxies are those for which it is easier to detect the gas emission at high galactic latitude and for which the column density is higher, even in the disk outskirts. The extraplanar gas is commonly defined as the detectable $H\alpha$ emission where the stellar continuum is not detected. This could be done from the continuum-subtracted emission-line image which delimits the stellar disc (e.g. Miller & Veilleux 2003; Rosado et al. 2013; Levy et al. 2019; Tomičić et al. 2021). This is typically what is done when observations with narrow- and broad-band filters around $H\alpha$ emission are combined. Alternatively, the old stellar disk in spiral galaxies (Population II stars) could be better defined from redder broad-band in the near-infrared (*NIR*, e.g. Kamphuis et al. 2007; Ho et al. 2016; Bizyaev et al. 2017, 2022) and young stellar population from bluer broad-band, e.g. in the *UV*, which traces the young stellar populations of ages up to tenths of Myrs (Hoopes et al. 2001; Thilker et al. 2007; Bianchi 2011; Kennicutt & Evans 2012). We used this method in this work. We present the $H\alpha$ emission maps of a sample of galaxies. The net $H\alpha$ maps (i.e. continuum free) were obtained using the scanning Fabry-Perot spectroimager (FP) GHASP, providing complete two-dimensional coverage of very extended line emission regions, ideal for studying the faint diffuse gas emission. We compared $H\alpha$ FP monochromatic maps with *NIR*, *NUV* and Far *UV* (*FUV*) images available in the literature. We defined a certain threshold in the *NIR* image under which the stellar density is low and consider that the eDIG is the $H\alpha$ emission below this limit. The geometric parameters of the galaxies, such as the isophotal position angle, peak light distribution and inclination, are obtained from the photometric analysis of the *UV* and *NIR* images, and will serve as reference when studying the $H\alpha$ kinematics in a forthcoming paper.

The paper is structured as follows. In Section 2, we provide details about the sample selection. In Section 3, we describe the data acquisition and reduction processes. In Section 4, we explain how the stellar disc and the extraplanar components are identified. In Section 5, we present the individual results of the photometric analysis of each galaxy in our sample. In Section 6, we discuss our main results. Finally, in Section 7, we provide a summary and the conclusions of our results. In order to compare our results with previous surveys, throughout this work we assumed a Hubble constant of $H_0 = 70 \text{ km s}^{-1} \text{ Mpc}^{-1}$ (e.g. Thilker et al. 2007; Ho et al. 2016; Levy et al. 2019).

2 THE SAMPLE SELECTION

Isolated galaxies have been the subject of selection and study for many decades. Evidences are accumulating that over at least a few billion years the evolution of isolated galaxies has not been driven by interactions with physically associated companions (see e.g. Verdes-Montenegro et al. 2005; Karachentseva et al. 2010; Karachentsev et al. 2011; Rampazzo et al. 2020, and references therein). In this sense, isolated galaxies are the ideal reference sample

¹ Sydney-AAO Multi-object Integral field spectrograph (SAMI)

² Mapping Nearby Galaxies at Apache Point (MaNGA)

³ Calar-Alto Legacy Integral Field Area (CALIFA)

⁴ Continuum haloes in Nearby Galaxies—an EVLA Survey (CHANG-ES)

Table 1. General parameters of the highly inclined isolated galaxies sample

CIG Name (1)	Other Name (2)	RA (J2000) (hh mm ss) (3)	Dec (J2000) (° ‘ ‘‘) (4)	V_{sys} (km s^{-1}) (5)	Distance (Mpc) (6)	i (deg) (7)	K_s (mag) (8)	$D_{25}(B)$ (kpc) (9)	Type (10)	S_{60} (Jy) (11)	S_{100} (Jy) (12)	L_{FIR} ($10^{43} \text{ erg s}^{-1}$) (13)
71	UGC 01391	01 55 15.8	+10 00 49.2	5901	84.3	83.8	10.8	35.4	Sc	0.66	1.38	6.79
95	UGC 01733	02 15 20.6	+22 00 22.0	4418	63.1	86.5	11.6	33.4	Sc-w	0.22	0.64	1.49
159	UGC 03326	05 39 37.1	+77 18 44.9	4121	58.9	85.4	9.6	60.8	*Scd:	1.10	3.57	3.26
171	UGC 03474	06 32 37.6	+71 33 39.5	3634	51.9	84.0	10.1	33.8	*Scd:	0.57	1.43	4.40
183	UGC 03791	07 18 31.8	+27 09 28.7	5090	72.7	80.4	11.4	26.0	*Sd :	0.49	1.38	2.78
201	UGC 03979	07 44 31.0	+67 16 24.9	4061	58.0	80.9	10.6	31.4	SA(rs)c	1.18	2.86	3.39
329	UGC 05010	09 24 55.1	+26 46 28.8	4096	58.5	81.3	9.3	42.8	SA(rs)b	0.30	1.34	1.61
416	UGC 05642	10 25 41.8	+11 44 20.8	2322	33.2	81.1	11.6	18.0	Sd -pec	0.52	1.16	2.69
593	UGC 08598	13 36 40.7	+20 12 00.5	4909	70.1	83.2	10.8	35.5	SBx(s)b:	0.09	0.40	0.53
847	UGC 11132	18 09 26.2	+38 47 39.9	2837	40.5	81.2	10.7	24.6	*Sb	0.59	1.98	5.74
906	UGC 11723	21 20 17.5	-01 41 03.6	4899	70.0	80.9	10.0	37.9	Sbc	1.97	5.95	11.51
922	UGC 11785	21 39 26.8	+02 49 37.6	4074	58.2	84.2	11.0	29.4	Scd-w	0.31	1.62	2.57
936	UGC 11859	21 58 07.4	+01 00 32.3	3011	43.0	85.7	11.4	38.7	Sc:	0.71	1.49	1.13
1003	UGC 12304	23 01 08.3	+05 39 15.7	3470	49.6	82.5	10.3	22.9	Scd	2.06	4.57	15.07

Columns: (1) CIG galaxy name; (2) UGC galaxy name; (3) and (4) wcs coordinates (J2000); (5) V_{sys} : systemic velocity from NED; (6) heliocentric distance to the galaxy; (7) i : inclination computed using the relation 1 (see the text); (8) K_s : apparent K_s -band magnitude from NED; (9) $D_{25}(B)$: optical diameter in the B -band from NED; (10) Hubble classification from Buta et al. (2019) and, if not available, from NED (*); (11) and (12) flux densities at $25 \mu\text{m}$, $60 \mu\text{m}$ and $100 \mu\text{m}$ in Jy from Lisenfeld et al. (2007); (13) FIR luminosity computed with the equation 4 (see Section 6.2).

to study internal galactic forces and galaxy morphological, dynamical and photometric evolution minimizing possible environmental effects.

The CIG catalogue (Karachentseva 1973) and its more recent revisions (Verdes-Montenegro et al. 2005; Verley et al. 2007b; Argudo-Fernández et al. 2013) are examples of a successful attempt to compile a sample of isolated galaxies. Historically, Karachentseva (1973) obtained her catalogue from the visual inspection of the *Digitized Sky Survey* (DSS) images of the 27 837 galaxies – and of their surroundings – (at Galactic latitudes $|b| \geq 20^\circ$) contained in the CGCG⁵. A list of 1050 galaxies were found to meet the isolation criterion she adopted (see also Karachentseva et al. 2010).

Since we are looking for the incidence of eDIG among isolated galaxies we have selected a sample from the CIG catalogue (Karachentseva 1973) of late-type galaxies (Spirals with morphological type > 5 , i.e. Sb to be checked) (see Buta et al. 2019) dominated by Population I stars that satisfy the following additional characteristics we derived from the NED data-base:

(i) galaxies with high inclination ($i \geq 80^\circ$) computed with the expression

$$i = \cos^{-1}(b/a), \quad (1)$$

where b and a are the apparent optical major and minor axes of the galaxy respectively;

(ii) galaxies with redshift $z \leq 0.02$ to ensure that the emission of the redshifted $\text{H}\alpha$ line fits in the optical wavelength;

(iii) galaxies with apparent K_s -band magnitude $K_s \leq 12$. The near-infrared is sensitive to nuclear rings and large-scale bars, which might fuel active nuclei (e.g. Kormendy & Illingworth 1982; Eskridge et al. 2002; Jarrett et al. 2003).

A complete sample of 14 nearby isolated late-type edge-on

galaxies was obtained (see Figure 1). General parameters of our galaxy sample are listed in Table 1.

Isolation degree

To be an isolated galaxy, the CIG catalogue required that no similar size neighbours were found close to the galaxy. This requirement can be described as follows: a galaxy with a standard angular diameter denoted as a_1 is classified as isolated when the angular separation X_{1i} between the galaxy and its i -th neighbor with angular diameter $a_i \in [0.25, 4] \cdot a_1$, meets or exceeds a threshold of $X_{1i} \geq 20 a_i$ (see equations 1 and 2 in Karachentseva et al. 2010). Since galaxies from the CIG catalogue were collected by visual inspection of DSS images, the companion galaxies are expected to be faint or mostly dwarf galaxies. Recently, the CIG catalogue has been refined using new quantification methods (e.g. Verley et al. 2007b) and modern tools like images with higher resolution than the plates of Palomar (e.g. Argudo-Fernández et al. 2013) and new images from H I emission data (e.g. Jones et al. 2018). In this Section, we discuss how effectively our galaxy sample selected from the CIG catalogue meets these new isolation checks. However, even if a subset of our sample does not meet the strictest isolation criteria, all galaxies in our sample still represent a significant part of the overall isolated galaxy sample.

In the frame of the long-term AMIGA project (Analysis of the interstellar Medium of Isolated GALaxies⁶), Verley et al. (2007a,b) revised all the positions of the CIG galaxies based upon the digitized photographic plates from POSS-1 and POSS-2 providing a quantification of the degree of isolation of CIG galaxies with the local number density of neighbour galaxies (η_k), and the tidal strength (Q_k) affecting the central galaxy by its neighbourhood. These parameters depend on the position, diameter and mass of the primary galaxy and its k -th neighbour. Thus, these parameters

⁵ *Catalogue of galaxies and of clusters of galaxies* (CGCG, Zwicky et al. 1968) <https://cdsarc.cds.unistra.fr/viz-bin/cat/VII/190>.

⁶ Analysis of the interstellar Medium of Isolated GALaxies (AMIGA) (<http://www.iaa.es/AMIGA.html/>)

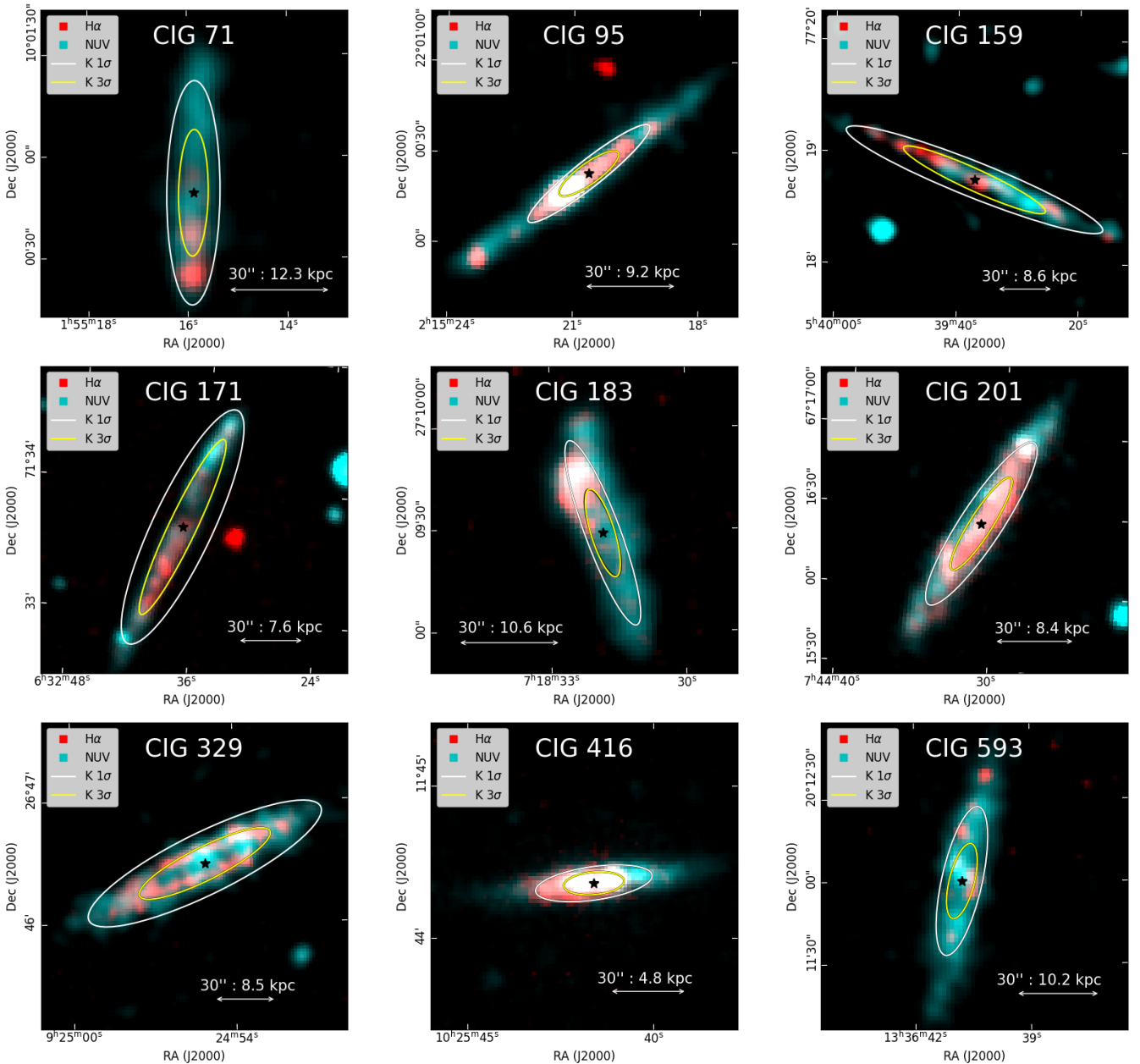


Figure 1. Superposition of the respective FP $H\alpha$ monochromatic map and GALEX NUV image of the galaxies in our sample. The ellipses fitted to the surface brightness level at 1σ (white) and 3σ (yellow) of the typical background noise (see e.g. Jarrett et al. 2000) of the respective 2MASS K_s -band image are overlain on the respective map. To distinguish the extraplanar material of each galaxy, the old stellar disc plane is traced by the ellipse fitted to the 3σ surface brightness level. We have masked the nearest and brightest field stars to each galaxy in the UV -band images. At the distance of each galaxy (see Table 1) the kpc measure equivalent to 30 arcsec is indicated with an arrow.

provide a clear picture of the environment around the isolated galaxies: the presence of one single similar size neighbour at a small distance to the CIG galaxy would result in a high value of the tidal strength (Q_k) estimation, while the local number density (η_k) remains quite low as it is averaged over more nearest neighbours (Verley et al. 2007b). In Table 2 we list the number of neighbours and the nearest-neighbour distance to each galaxy in our sample according to Verley et al. (2007a). Then, Argudo-Fernández et al. (2013) re-evaluated the isolation criteria of AMIGA galaxies within a field radius of 1 Mpc using both photometric and spectroscopic

data available from the *Sloan Digital Sky Survey* (SDSS) to refine the η_k and Q_k parameters.

Figure 2 shows the comparison between the local number density (η_k) and tidal strength (Q_k) of the galaxies in our sample making the distinction between the results of Verley et al. (2007b) and Argudo-Fernández et al. (2013). From Figure 2 and Table 2, we observe that some galaxies classified as isolated in the AMIGA sample have its nearest neighbour at an angular distance of twice or three times their optical diameters, for example CIG 171 and 201. According with Verley et al. (2007a), most of the neighbouring galaxies of CIG galaxies have a diameter $\leq 0.25a_1$, implying

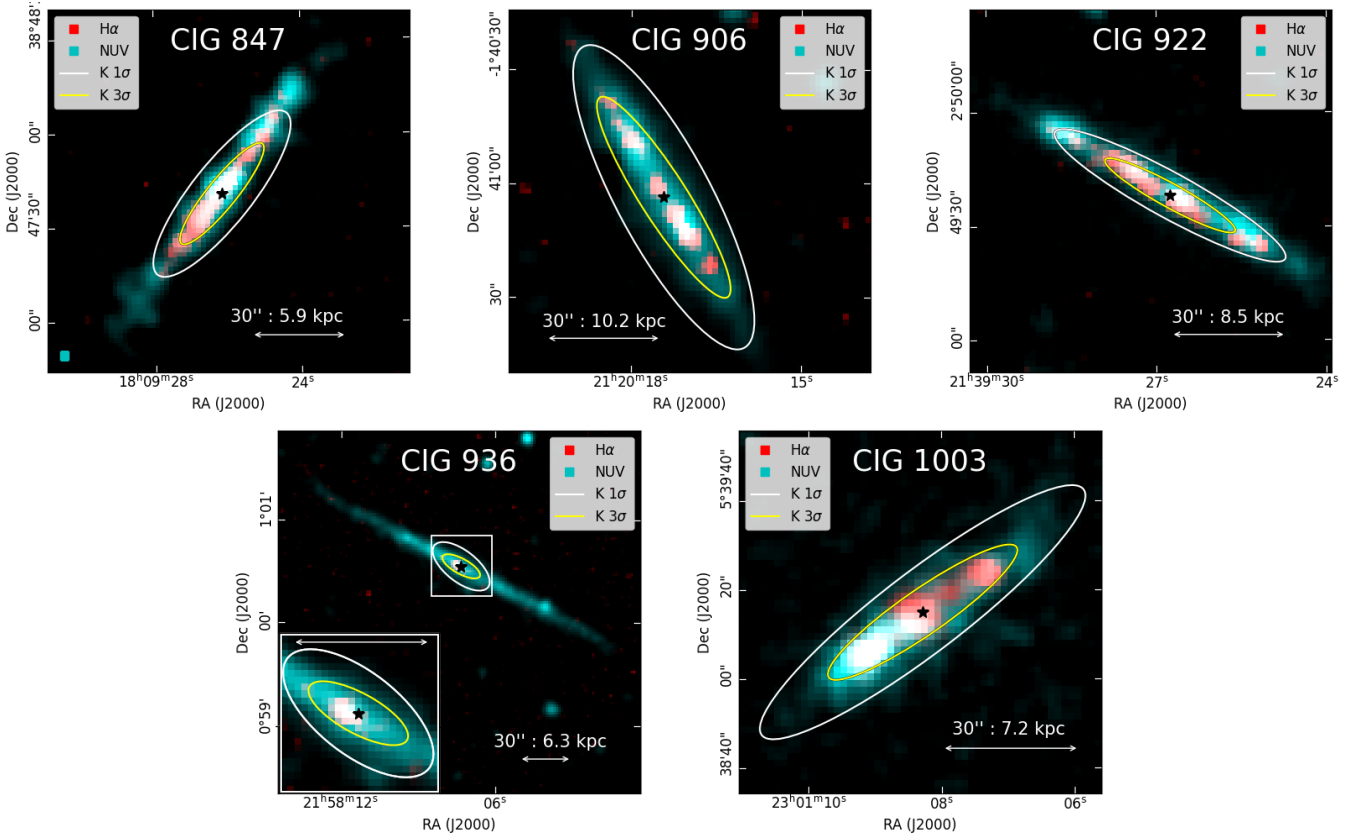


Figure 1. Continue.

they are dwarf companions which were not taken into account by Karachentseva (1973) when collecting the CIG catalogue but perhaps they can influence the evolution of the main galaxy. Therefore, if CIG 171 and 201 are in region of bona fide isolated galaxies in the AMIGA sample, we may infer that the nearest neighbours are small enough to not exert significant gravitational perturbations on the main galaxy. On the other hand, Verley et al. (2007b) had already determined that the galaxies of our sample, CIG 71 and CIG 936, were outside this region, excluding both galaxies from the AMIGA sample. As Argudo-Fernández et al. (2013) improved the quantification of the isolation degree, another galaxy of our sample, CIG 1003, is also out of the area of isolated galaxies in the $Q_k - \eta_k$ plane. In this way, 3 out of 14 galaxies in our sample failed the isolation criteria of the AMIGA sample, probably because they have some faint companions previously undetected by Karachentseva (1973).

Later, Jones et al. (2018) provided integrated H I fluxes of AMIGA galaxies by presenting a catalogue of H I single dish observations. With these new data, Jones et al. (2018) included a review of integral features of AMIGA galaxies allowing to ensure isolation level of the AMIGA catalogue. Since the Argudo-Fernández et al. (2013) work is limited to the SDSS data, Jones et al. (2018) adopted the criteria of Verley et al. (2007b), and excluded all sources with heliocentric velocities below 1500 km s^{-1} , removed all dwarf galaxies that were in the CIG, and discarded all sources with potentially spurious spectral parameters, leaving a final sample of 544 CIG galaxies. In these terms, 8 out of 14 galaxies in our sample would not be considered well isolated: CIG 71, 159, 171, 201, 416, 922, 936 and 1003.

While some members of our sample, selected from the CIG

catalogue (Karachentseva 1973), may not fully meet the strictest current isolation criteria, it is important to stress that all galaxies in our sample are still classified as isolated galaxies. The different arguments stated above make us aware of the different degrees of isolation of the galaxies in our sample. However, previous studies indicate that late-type galaxies are usually located in very low-density environments. In this context, we decided not to exclude any galaxy a priori but rather discuss each of them knowing their isolation properties.

3 THE DATA

3.1 H α observations and data reduction

Observations of the H α emission line were performed using the scanning Fabry-Perot (FP) interferometer, GHASP, attached at the Cassegrain focus of the 1.93m telescope at the *Observatoire de Haute-Provence* (OHP, see Table 3). A GaAs Image Photon Counting System (IPCS) is used to reach low detection levels, offering a total FoV of about $5.8 \times 5.8 \text{ arcmin}^2$ with a pixel scale of $\sim 0.68 \text{ arcsec pix}^{-1}$ (Gach et al. 2002). Since the IPCS has no readout noise, exposures of 10 seconds were chosen for each of the 32 scanning steps required to cover the GHASP's free spectral range (FSR). In order to detect the eDIG emission, the scanning sequence was typically repeated ~ 35 times, resulting in a total exposure time per galaxy of $\sim 180 \text{ min}$. We used narrow-band interference filters (mainly $\text{FWHM} \approx 15 \text{ \AA}$ and in a few cases slightly larger up to 24 \AA) enabling to select the redshifted H α line of ionized hydrogen (6562.78 \AA). The scanning Fabry-Perot interferometer we used, with

Table 2. Number of neighbours of galaxies in our sample and the distance to the nearest one measured by Verley et al. (2007a).

CIG Name	Neighbours	Distance	
		(arcsec)	(kpc)
(1)	(2)	(3)	(4)
71	4	941	384.6
95	71	362	110.7
159	34	456	130.2
171	91	152	38.2
183	25	784	276.3
201	57	109	30.6
329	101	316	89.6
416	168	362	58.3
593	26	739	251.2
847	79	644	126.4
906	28	391	132.7
922	97	197	55.6
936	88	234	48.8
1003	77	118	28.4

Columns: (1) CIG galaxy name; (2) number of neighbours in a physical radius of 0.5 Mpc; (3) and (4) distance to the nearest neighbour in arcseconds and kpc respectively given the heliocentric galactic distance listed in Table 1.

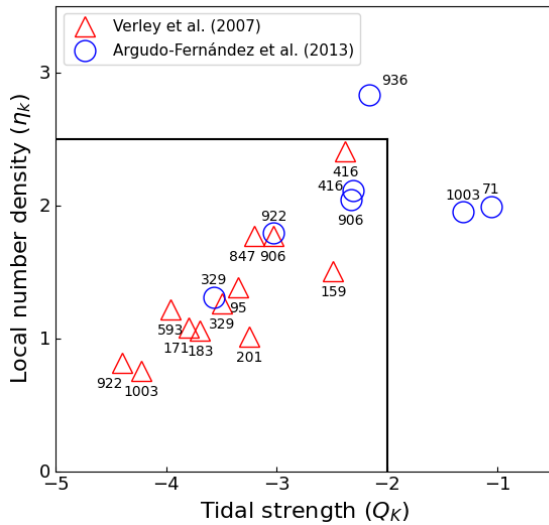


Figure 2. Comparison between the local number density (η_k) and tidal strength (Q_k) parameters for the CIG galaxies in our sample. These parameters were obtained first, based on digitized photographic plates from POSS-1 and POSS-2 (Verley et al. 2007b,a) (red triangles) and later, on available photometric and spectroscopic data from SDSS-DR9 (Argudo-Fernández et al. 2013) (blue circles). The CIG catalogue numbers are indicated on top the circles and below the triangles. According to Verley et al. (2007b), the horizontal ($\eta_k = 2.4$) and vertical ($Q_k = -2$) lines enclose the region of bona fide isolated galaxies in the AMIGA sample.

an interference order of $p \simeq 798$ and a finesse $\mathcal{F} \simeq 13$ at $H\alpha$, allowed GHASP to reach a typical spectral resolution of $R \sim 10\,000$.

Two calibration cubes were obtained, one at the beginning and another at the end of the observation, using a neon lamp with selected narrow line at 6598.95 \AA , close to the redshifted nebular wavelength in order to minimize phase shift effect (e.g. Gómez-López et al. 2019). The observation date, filter’s central wavelength and FWHM,

the total exposure time and the astronomical seeing of each galaxy are listed in Table 4.

For the data reduction, we used the packages based on homemade IDL⁷ routines, REDUCWIZARD and COMPUTEVERYTHING (see e.g. Epinat et al. 2008). The data reduction technique has been widely reported in Daigle et al. (2006b). In summary, it consists in the following steps: (1) integration with guiding correction of the total data cubes obtained during the observation; (2) application of a Hanning spectral smoothing on the data cube; (3) calibration in wavelength of the integrated data cubes through the computation of a parabolic phase map which is computed from the calibration cube in order to obtain the reference wavelength for the line profile observed inside each pixel, creating a wavelength-sorted data cube by applying the phase map correction to the interferogram data cube; (4) subtraction of the OH sky-lines emission; (5) a Gaussian spatial smoothing with a FWHM selected on the wavelength data cubes; and (6) computation of $H\alpha$ monochromatic, continuum, radial velocity and velocity dispersion maps for each wavelength calibrated cube. Finally, astrometric information was attached to the processed files by using the IDL task KOORDS from the KARMA package (Gooch 1996). In Table 4, we also listed the seeing and the final spatial resolution in kpc arcsec⁻¹ after the spatial Gaussian smoothing of the $H\alpha$ maps.

We performed two separate processes on the wavelength data cube. First, we applied Gaussian spatial smoothing, and then, independently, we performed adaptive spatial binning using a Voronoi tessellation with a target SNR $\simeq 5$. To ensure a signal-to-noise ratio SNR ≥ 5 in the Gaussian smoothed data cube, we compared the monochromatic $H\alpha$ maps derived from both processes and set a threshold for the emission detected in the Gaussian smoothed maps. For a SNR $\simeq 5$, the GHASP surface brightness detection limit is $F = 2.5 \times 10^{-17} \text{ erg sec}^{-1} \text{ cm}^{-2} \text{ arcsec}^{-2}$ (see Epinat et al. 2008; Gómez-López et al. 2019; Sardaneta et al. 2022). As no $H\alpha$ calibrated image of any galaxy in our sample has been previously published, we followed the calibration procedure outlined by Epinat et al. (2008) to determine the total $H\alpha$ flux for the GHASP data (see Appendix B).

The data analysis was made with the program ADHOCw⁸, IRAF⁹ tasks, the SAO Image DS9 software¹⁰ and our own PYTHON scripts.

3.2 Archival data

The DSS is available at the site of the *Space Telescope Science Institute* (STScI)¹¹. The DSS $6.5 \times 6.5 \text{ deg}^2$ plates have been scanned using a modified PDS microdensitometer with a binned pixel scale of about $\sim 1.0 \text{ arcsec pix}^{-1}$. In this work, we use the DSS R-band images ($5900\text{--}7150 \text{ \AA}$) of our galaxy sample as a reference to provide

⁷ Interactive Data Language, ITT Visual Information Solutions: <https://www.l3harrisgeospatial.com/Software-Technology/IDL>

⁸ ‘Analyse et Depouillement Homogene des Observations Cigale for Windows’ <http://cesam.lam.fr/fabryperot/index/softwares> developed by J. Boulesteix at Marseille Observatory in 2005.

⁹ ‘Image Reduction and Analysis Facility’ <http://iraf.noao.edu/>

¹⁰ SAO Image DS9. An image display and visualization tool for astronomical data (Joye & Mandel 2003) <https://sites.google.com/cfa.harvard.edu/saoimageds9>

¹¹ The Digitized Sky Surveys were produced at the Space Telescope Science Institute under U.S. Government grant NAG W-2166. The images of these surveys are based on photographic data obtained using the Oschin Schmidt Telescope on Palomar Mountain and the UK Schmidt Telescope. The plates were processed into the present compressed digital form with the permission of these institutions. https://archive.stsci.edu/cgi-bin/dss_form

Table 3. Instrumental and observational parameters

Parameter	Value
Telescope	1.93 m OHP
Aperture ratio of the focal reducer	$f/3.9$
Instrument	GHASP
Detector type	IPCS GaAs system
Detector size (pix ²)	512×512
Image scale (arcsec pix ⁻¹)	0.68
Field of view (arcmin ²)	5.9×5.9
Interference order at H α	798
FSR at H α (Å / km s ⁻¹)	8.23 / 376
Finesse observed	~13
Resolution	~ 10000
Spectral sampling at H α (Å / km s ⁻¹)	~0.26 / ~11.5

a large-band optical view of the target. However, we do not calibrate these images in flux since their zero-point magnitude is currently unknown. The average seeing obtained from the image headers was ~1.5 arcsec.

The *Two Micron All-Sky Survey* (2MASS, Jarrett et al. 2000) project uses two highly-automated 1.3 m telescopes, one at Mt. Hopkins, Arizona, and the other at Cerro Tololo, Chile. Each telescope is equipped with a three-channel camera, each channel consisting of a 256×256 pix² array of HgCdTe detectors, capable of observing the sky simultaneously at J (1.24 μ m), H (1.66 μ m) and K_s (2.16 μ m) near-infrared bands with an angular resolution of 2.0 arcsec and a pixel size of 1.0 arcsec pix⁻¹. Owing to the transparency of interstellar dust within the galaxies and to the dominance of late-type stellar populations in producing galactic near-infrared flux, the 2MASS galaxy images trace the overall stellar mass distribution in these galaxies¹². To calibrate in flux, the zero-point conversion values are published in the *Explanatory Supplement to the 2MASS All Sky Data Release and Extended Mission Products*¹³. In this work we use the K_s -band images of the nearby isolated late-type edge-on galaxies selected to sketch the stellar Population II.

Galaxy Evolution Explorer (GALEX) was the first ultraviolet (UV) all-sky survey covering a field of view (FoV) of ~ 1.25 deg using microchannel plate detectors to obtain direct images in the NUV ($\lambda_{\text{eff}} = 2271$ Å) and FUV ($\lambda_{\text{eff}} = 1528$ Å) with a resolution of 4.2/5.3 arcsec (FUV/NUV) and a pixel scale of 1.5 arcsec pixel⁻¹ (Bianchi 2011)¹⁴. Conversion values between GALEX count rates, fluxes, and AB magnitudes are available in the *GALEX Guest Investigator Web Site*¹⁵. We use GALEX- NUV and FUV images as tracers of stellar Population I in galaxies in our sample.

Thus, in this work we study H α , NIR , and UV images, each one with different resolutions. In the case of the H α emission data, the seeing conditions varied across the sample of galaxies, with different galaxies experiencing different levels of atmospheric turbulence due

to the diversity of observational conditions during data gathering (see Table 4). For example, the closest galaxy, CIG 71, experienced the worst seeing conditions with a resolution of ~4.4 arcsec (1.8 kpc), as did the most distant galaxy, CIG 416, with a resolution of ~4.1 arcsec (0.7 kpc). However, CIG 922, a galaxy located at an average distance, had relatively average seeing conditions with a resolution of ~2.2 arcsec (0.6 kpc). The seeing for the NIR (2 arcsec) and NUV/FUV (4.2/5.3 arcsec) images is considered constant for the whole sample. However, it is important to be aware that the different seeing disc sizes combined with the different distances of the galaxies blur the data and impact the spatial physical resolution making it more difficult to distinguish fine details such as eDIG filaments or patches.

Finally, since the *Infrared Astronomical Satellite* (IRAS) satellite did not cover the whole sample of CIG galaxies, Lisenfeld et al. (2007) reprocessed the IRAS MIR/FIR survey data using the ADDSCAN/SCANPI utility for 1 030 out of 1 050 CIG galaxies as part of the AMIGA project. In this work, we use the IR flux densities at 60 and 100 μ m from AMIGA survey (see Table 1).

4 IDENTIFYING THE STELLAR DISC

To disentangle the galactic disc from the gaseous extraplanar component, we performed a photometric analysis of the 2MASS 2.2 μ m image, tracer of the old stellar population, and of the GALEX NUV and FUV images, connected to the young stellar population in the galaxy. Because of the particular characteristics of the images in each band, to derive the surface brightness profile, we used two different software packages, the `ELLIPSE` task from the IRAF STSDAS package (Jedrzejewski 1987) and the `ISOPHOTE` package from the PYTHON PHOTUTILS package¹⁶ (Bradley et al. 2020). Both programs fit an ellipse via an iterative method (devised by Jedrzejewski 1987) as well as quantify the distortion from a perfect ellipse by means of higher-order Fourier harmonics:

$$\mu(\theta) = \mu_0 + \sum_{n=1}^4 (A_n \sin n\theta + B_n \cos n\theta), \quad (2)$$

where μ_0 is the surface brightness averaged over the ellipse as a function of the azimuthal angle θ and, A_n and B_n the higher order Fourier coefficients. The first- and second-order coefficients (A_1 , B_1 , A_2 , B_2) indicate the errors in the fitting procedure, being zero for a best-fit ellipse, while the third-order coefficients (A_3 , B_3) characterize the deviation of the fitted ellipse from the isophote shape. The coefficient B_4 measures symmetric distortions from pure ellipticity: when $B_4 > 0$, the isophotes have a ‘disc-like’ (circular) shape and, when $B_4 < 0$, the isophotes have a ‘boxy’ (rectangular) shape. The inclination angle (i) with respect to the sky-plane of the galactic disc can be measured through the ellipticity (ϵ) of the fitted ellipse. Using diverse tracers of the stellar population serves as a crucial means to differentiate between the particular cases presenting UV extended discs or UV haloes which represent at least one-third of the galaxies in the local universe (Thilker et al. 2007) and, as we will show for our sample in Section 5, approximately two-thirds of the late-type isolated high-inclined galaxies.

The analysis of edge-on galaxies is more difficult than the analysis

¹² 2MASS Data Release Documentation <https://irsa.ipac.caltech.edu/data/2MASS/docs/releases/docs.html>

¹³ Section VI.4.a of the *Explanatory Supplement to the 2MASS All Sky Data Release and Extended Mission Products*: https://www.ipac.caltech.edu/2mass/releases/allsky/doc/sec6_4a.html

¹⁴ *Galaxy Evolution Explorer* (GALEX) <http://www.galex.caltech.edu/index.html>

¹⁵ Section Instrument and Calibration of the *GALEX Guest Investigator Web Site*: https://asd.gsfc.nasa.gov/archive/galex/FAQ/counts_background.html

¹⁶ PHOTUTILS is an open source PYTHON package affiliated of Astropy that primarily provides tools for detecting and performing photometry of astronomical sources. <https://photutils.readthedocs.io/en/stable/index.html> <https://photutils.readthedocs.io/en/stable/api/photutils.isophote.Ellipse.html>

Table 4. Journal of observations

CIG Name (1)	Date (aaaa/mm/dd) (2)	λ_c (Å) (3)	FWHM (Å) (4)	t_{exp} (min) (5)	Seeing (arcsec) (6)	Resolution (kpc arcsec ⁻¹) (7)
71	2019/10/26	6700	24	176	4.4	2.0
95	2019/10/27	6665	15	192	2.4	1.0
159	2021/01/13	6655	15	181	2.6	1.0
171	2021/01/14	6645	15	187	2.8	0.9
183	2021/01/21	6675	15	213	3.0	1.3
201	2021/01/16	6655	15	187	3.3	1.1
329	2021/01/13	6655	15	181	3.8	1.2
416	2021/01/21	6615	15	187	4.1	0.7
593	2021/03/09	6675	15	219	2.9	1.2
847	2019/10/29	6630	20	187	2.3	0.6
906	2019/10/26	6675	15	187	1.9	0.9
922	2019/10/25	6655	15	192	2.2	0.8
936	2019/10/27	6630	20	187	3.0	0.8
1003	2019/10/26	6645	15	187	2.5	0.8

Columns: (1) CIG galaxy name; (2) date of observation; (3) λ_c : non-tilted filter central wavelength; (4) FWHM: non-tilted full width half-maximum; (5) t_{exp} : total exposure time; (6) Seeing in arcs; (7) Final spatial resolution in kpc per arcseconds after having applied a spatial Gaussian smoothing on the $H\alpha$ wavelength data cubes (see Section 3.1).

of galaxies with lower inclination because the high inclination affects the apparent shape of the galaxy along the line of sight (LoS). In photometric analysis of low-inclination galaxies, a smooth bulge-disc transition is typically observed in the resulting plots (e.g. Marino et al. 2010). However, in highly inclined galaxies, the brightness of the inner regions is dominated by the bulge with a small contribution from the thin disc. As the radius increases, the contribution from the disc becomes more important, leading to an abrupt bulge-disc transition in the resulting plots. This provides a noisier behaviour at small radii in the photometric analysis for highly inclined galaxies.

Considering that in late-type galaxies old and young stellar populations are mixed in the disc (e.g. Nersesian et al. 2019), we define the stellar homogeneous disc by using the ellipse delimiting the locus of the stars belonging to the old stellar population since they trace the bulk of the mass and probe the global potential of the disc galaxy.

4.1 NIR emission

For the 2MASS 2.2 μm image, we applied the method of elliptical isophote fitting using the task ELLIPSE (Jedrzejewski 1987) from the IRAF STSDAS package. As initial parameters we set the galaxy coordinates as the centre, the B -band optical diameter (D_{25}) as the maximum semi-major axis length, and the optical position angle (PA) and ellipticity (ϵ) published in the NED (see Table 1). We used logarithmic radial sampling with an initial step of ~ 0.5 pixel along the semimajor axis in order to derive the surface brightness profile of each galaxy in an iterative process. The centre, PA, and ellipticity of the ellipse were allowed to vary in each iteration.

Jarrett (2000) defined the isophotal aperture r_{20} , derived from the K_s -band isophote at $\mu_K = 20 \text{ mag arcsec}^{-2}$, as the 2MASS standard aperture, corresponding to roughly 1σ of the typical background noise in the K -band images. However, because of the high levels of background noise in the 1-2 μm atmospheric windows, the 2MASS is not as sensitive to low surface brightness emission from galaxies (Jarrett 2000). In consequence, the K_s -band benchmark of $\mu_K = 20 \text{ mag arcsec}^{-2}$ elliptical isophote aperture might underestimate the total flux between 10% and 20%, depending on the radial

distribution according to the Hubble type (Jarrett 2000; Jarrett et al. 2003). On the other hand, discrepancies in the measurements at the $\mu_K = 20 \text{ mag arcsec}^{-2}$ level between the 2MASS and other K_s -band surveys (see e.g. Fingerhut et al. 2010) have suggested potential errors in the 2MASS data reduction process. In fact, Jarrett (2000) explained that systematic components such as H -band airglow variations were not well understood by then and might have induced large errors in the photometry¹⁷. Consequently, the choice of a brighter isophote to define the galactic disc boundaries, beyond the 1σ level at $\mu_K = 20 \text{ mag arcsec}^{-2}$, may help to mitigate potential data reduction errors in the 2MASS data set.

To be consistent with previous optical photometric results, Jarrett et al. (2003) derived some galactic properties from the 3σ isophote, such as the ellipticity (ϵ) and position angle (PA), in the 2MASS *Large Galaxy Atlas* (LGA) and the 2MASS *Extended Source Catalogue*. These photometric parameters are consistent with our K_s -band results as well (see Table 5). Furthermore, the K_s elliptical isophotal photometry should include the core, bulge, and disk components, capturing most of the flux from a galaxy (e.g. Jarrett et al. 2000). Therefore, to ensure that a significant portion of the galaxy's light is captured and to avoid empty sky background noise, hereafter we use the ellipse at 3σ on the background as reference for the disc traced by the stellar Population II. Although this value may not represent the true galactic radii, it is a practical starting point to define the old population stellar disc boundaries.

The older stellar population in spiral galaxies points out internal structures such as spiral arms, bulges, warps, rings, and bars (Jarrett et al. 2003). Bars play a major role in the secular evolution of galaxies and, through vertical resonances, drive stars above the plane to form peanut/box-shaped pseudo-bulges (Combes & Sanders 1981a). The non-axisymmetry of the bars produces the gas to flow inwards

¹⁷ Explanatory Supplement to the 2MASS All Sky Data Release and Extended Mission Products IV <https://www.ipac.caltech.edu/2mass/releases/allsky/doc/explsup.html>. 2MASS Data Processing. 5. Extended Source Identification and Photometry https://www.ipac.caltech.edu/2mass/releases/allsky/doc/sec4_5e.html

Table 5. Photometric parameters resulting from the ellipse fitting to the 2MASS K_s -band and GALEX NUV and FUV images.

CIG Name	K_s -band, 1σ			K_s -band, 3σ			NUV			FUV		
	r (arcsec)	PA (deg)	ε	r (arcsec)	PA (deg)	ε	r (arcsec)	PA (deg)	ε	r (arcsec)	PA (deg)	ε
(1)	(2)	(3)	(4)	(5)	(6)	(7)	(8)	(9)	(10)	(11)	(12)	(13)
71	33.1	179.1	0.76	18.7	178.8	0.77	61.0	177.9	0.80	34.6	177.9	0.84
95	25.6	128.8	0.83	12.0	126.2	0.71	73.3	127.3	0.85	60.2	126.4	0.90
159	74.4	68.9	0.87	42.0	66.2	0.860	114.0	67.0	0.90	53.1	71.0	0.90
171	59.1	159.9	0.77	44.4	159.7	0.858	110.9	156.9	0.83	64.9	160.0	0.90
183	28.9	19.8	0.82	13.5	16.6	0.74	66.2	19.8	0.72	48.8	18.0	0.73
201	36.4	150.9	0.78	20.5	151.7	0.79	85.8	151.2	0.69	81.6	151.6	0.86
329	63.6	115.1	0.76	35.9	115.4	0.77	86.8	110.0	0.79	71.3	113.0	0.80
416	23.2	97.9	0.75	11.9	95.0	0.63	59.7	97.8	0.43	48.3	97.1	0.78
593	27.8	167.0	0.73	14.1	165.5	0.67	73.5	165.0	0.81	44.8	168.0	0.75
847	33.1	140.8	0.71	20.5	140.2	0.77	87.5	142.0	0.73	76.7	142.0	0.87
906	45.0	28.3	0.72	31.3	32.8	0.80	60.6	35.0	0.63	52.3	31.8	0.88
922	34.7	61.1	0.83	19.6	60.0	0.84	72.1	61.5	0.82	55.4	61.5	0.88
936	19.8	52.3	0.58	12.3	61.6	0.64	111.7	61.0	0.86	71.4	61.1	0.90
1003	45.5	127.3	0.80	25.7	124.7	0.80	52.8	129.4	0.54	53.3	119.4	0.81

CIG galaxy name listed in column (1). Major axis length (r), position angle (PA) measured from the North to the East and ellipticity (ε) of the ellipses fitted to the K_s -band image at 1σ level on the background are listed in columns (2), (3) and (4), respectively, and at 3σ level in columns (5), (6) and (7). Same parameters determined for the NUV image are listed in columns (8), (9) and (10), and for the FUV image in columns (11), (12) and (13).

fuelling SF in the central regions of their host galaxies (see e.g. Kim et al. 2021, and references therein). Bottom frame of panel (d) of Figure 3, and from Figures E1 to E13, shows the variation of the B_4 parameter with respect to the galactic semi-major axis (radius). From these graphics, we found that the only one galaxy in our sample that presents a coefficient $B_4 < 0$ is CIG 329 (see Figure E6) implying it has a ‘boxy’ bulge.

4.2 UV emission

The `ELLIPSE` task from IRAF works in an iterative manner, if there is contamination such as stars and H II regions or regions of too low SNR, the program continues generating ellipses but it outputs parameters with undefined values. To overcome this difficulty, other fitting software was used to derive the surface brightness profiles of the NUV and FUV images. The `ISOPHOTE` package from `PHOTUTILS` (Bradley et al. 2020), provides tools to fit elliptical isophotes to a galaxy image using an iterative method described by Jedrzejewski (1987) (see equation 2) for each ellipse as well. The `ISOPHOTE` package can also work in an iterative manner by measuring a maximum acceptable relative error in the local radial intensity gradient (typically 0.5). However, when two consecutive isophotes exceed the value specified by the parameter the program prevents ellipses either from prematurely stopping due to the stellar contamination or from growing in low SNR regions. Nonetheless, if the maximum semimajor axis is specified, the intensity gradient is set to ‘none’ and the algorithm proceeds inwards to the galaxy centre. Although it is not the general case and may not be the best fit, this procedure allows to analyse data with too low SNR in the inner regions of the galaxy, such as in some GALEX NUV and FUV images of galaxies in our sample. This fit algorithm is quite sensitive to the initial guesses. The iteration begins by giving a fixed semimajor axis length selected initially to grow linearly with steps of 0.5 pix and specifying the initial value of the galactic centre, PA and ε , then the algorithm proceeds to fit isophotes inwards to the galaxy centre.

We initialized the fitting parameters using the galaxy coordinates as the centre, the optical PA and ellipticity obtained from the NED

database, and the B -band optical diameter (D_{25}) as the maximum length of the semi-major axis obtained from the NED database (see Table 1). To overcome any discrepancies between the optical and UV radii, we made adjustments to the initial parameters by comparing the UV radius measured using the DS9 image analysis software with the optical radius, and modifying the corresponding initial parameter values if the optical radius was smaller than the UV radius. For most of our targets, we allowed the centre position, ellipticity and PA to vary during the fitting process. Some galaxies (CIG 71, 95, 847, 906 and 1003) present the NUV/FUV brightest knots beyond ~ 10 arcsec from the peak light distribution of the NIR emission, this last position is assumed the center of the galactic disc and it is probable that the NIR emission is shadowing the actual peak of the UV light. Hence, for these galaxies, we fixed the centre position at the NIR peak light distribution, assuming it indicates the galactic center, and we allowed the ellipticity and PA to vary during the fitting process. Thus, we ensure that the fitted ellipses accurately reflect the morphology of the target galaxies, taking into account any deviations from the ideal elliptical shapes.

We computed the isophotal radii at surface brightness levels of $\mu_{NUV,FUV} = 28 \text{ mag arcsec}^{-2}$ in NUV and FUV , which roughly correspond to the average surface brightness at the optical diameter (see e.g. Gil de Paz et al. 2007a; Marino et al. 2010; Cortese et al. 2012), using the limit AB magnitude in NUV of 20.08 mag and in FUV of 18.82 mag¹⁸.

4.3 Photometric and geometric parameters at different wavelengths

Photometric parameters, such as the PA and galaxy inclination, are useful observational constraints to reveal galaxy peculiarities when the galaxy configuration is examined, particularly when different wavelengths are considered. In Table 5 we list the photometric

¹⁸ GALEX Guest Investigator Web Site https://asd.gsfc.nasa.gov/archive/galex/FAQ/counts_background.html

parameters resulting from the ellipse fitting process. Panel (g) of Figure 3 and Figures E1 to E13 shows the surface brightness profiles of GALEX *NUV* and *FUV* images, while the resulting ellipses were overlaid on the *NUV* (panel e) and *FUV* (panel f) images, respectively (see for example Figure 3). The 1σ *NUV* and *FUV* isophotes computed after applying a Gaussian spatial smoothing of $\sigma \approx 4.5$ arcsec (3 pix) on the *NUV* and *FUV* images were overlaid on the H α monochromatic map (panel a) in order to allow a better comparison of the morphology traced at different wavelengths.

Inclination plays a critical role in the analysis of galaxy structure as it is used to correct its main parameters as the brightness (e.g. Stone et al. 2021) and the rotation velocity (e.g. Epinat et al. 2010). Assuming that the image of a spiral galaxy is the projection of a disc with the shape of an oblate spheroid, the inclinations of spiral galaxies can be roughly derived from the ellipticity of apertures used for photometry. If the thickness of a disc is neglected the relation between the inclination (i) to the celestial plane and the apparent diameter ratio can be described using the relation 1. If the thickness is taken in consideration, the inclination can be estimated using the expression:

$$\cos^2 i = \frac{(1 - \varepsilon)^2 - q_0^2}{1^2 - q_0^2}, \quad (3)$$

where $\varepsilon = 1 - b/a$ is the ellipticity at the isophotal radius and $q_0 = c/a$ is the flattening, in this case a , b and c are the three spheroid's axes (see e.g. Barbosa et al. 2015). Many works have shown that the flattening is type dependent (see e.g. Haynes & Giovanelli 1984). In this sense, Hall et al. (2012) determined an intrinsic flattening for spiral galaxies, $q_0 = 0.13$, by studying the relationship between the axial ratios in the i -band versus the $g - i$ galaxy colour computed at the effective radius for 871 edge-on galaxies from the SDSS. They showed that, although q_0 increases with redder, progressively bulge dominated galaxies, the q_0 distribution was rather flat for late-type galaxies only with an upturn in the transition between Sa to S0 galaxies.

Nonetheless, deriving the inclination from ellipticity may be problematic. For instance, prominent bulges can dominate the axial ratio measurement or in other cases, galaxies may not be axially symmetric owing to tidal effects or high surface brightness bars embedded in low surface brightness discs (Epinat et al. 2008, 2010; Hall et al. 2012; Kourkchi et al. 2019; Stone et al. 2021). All these rather common configurations can lead to large errors. Some solutions have been proposed, for example, in order to avoid contamination due to clumps of star formation, Epinat et al. (2010) suggested that the inclination should be preferentially derived from broad-band images with high resolution, as in the *NIR* rest frame of the galaxy tracer of the old stellar disc.

In addition to photometric techniques, to compute the galaxy inclination, some studies use visual inspection to evaluate the inclinations. For example, to select the high inclined galaxies from SDSS and CALIFA surveys, Bizyaev et al. (2017) and Levy et al. (2019), respectively, used the visibility of the dust lane in optical images of the galaxies to confirm the edge-on nature of the galaxies, excluding galaxies with dust lanes that were not centred in the midplane or displaying any visible track of spiral arms, bars, or other features. Kourkchi et al. (2019) evaluated this technique by designing an online graphical tool, achieving uncertainties of $\pm 4^\circ$ and suggesting to replace the human eye with a machine learning algorithm to compute more accurate inclinations.

In this work, the galactic inclination i was one of the selection parameters (see Section 2) for our sample. Firstly, the inclination of the CIG galaxies in our sample was computed by the relation 1

Table 6. Inclinations computed with different methods and wavelengths.

CIG	i_{Optic}		$i_{\text{NIR}, 1\sigma}$	$i_{\text{NIR}, 3\sigma}$	i_{NUV}
	(2)	(3)	(4)	(5)	(6)
71	83.8	...	78.4	78.6	81.2
95	86.5	...	83.3	75.0	85.4
159	85.4	...	90.0	86.9	90.0
171	84.0	...	78.7	86.6	83.7
183	80.4	84.0	82.9	76.9	75.5
201	80.9	84.8	79.9	80.6	73.6
329	81.3	85.5	78.4	79.1	80.4
416	81.1	85.2	77.4	69.3	56.0
593	83.2	...	76.4	72.3	81.7
847	81.2	85.4	74.6	79.2	76.2
906	80.9	84.8	75.7	81.3	69.6
922	84.2	...	83.5	84.6	82.6
936	85.7	...	66.6	70.2	86.4
1003	82.5	89.1	81.1	81.5	63.5

Column (1): CIG name. Column (2) and (3): inclination computed assuming a flat disc (see equation 1) and taking into account the galactic thickness (see equation 3) respectively, using the optical ellipse's semi-axes available in NED in both cases. Columns (4), (5), (6) and (7) inclination computed taking into account the galactic thickness (see the relation 3), using the ellipses fitted to the 1σ and 3σ level of the *NIR* image and to the one fitted to the brightness level $\mu_{\text{NUV}} = 28$ mag arcsec $^{-2}$ of the *NUV* image. In column (3), by using the flattening constant $q_0 = 0.13$ determined by Hall et al. (2012), the lower limit of ellipticity $1 - \varepsilon = 0.13$, for which equation 3 is valid, is exceeded by some of the galaxies in our sample in the optical band.

using the galactic apparent major and minor axes from the optical wavelength published in the NED. Next, we computed the inclinations of galaxies in our sample applying the relation 3, for the the 2.22 μm and *NUV* emission images we employed the ellipticity obtained from the ellipse fitting performed to them, and for the optical wavelength image, we used the galactic apparent major and minor axes from the NED. In all cases, we used the constant flattening $q_0 = 0.13$ determined by Hall et al. (2012). In the case of the *NIR* image we have computed the inclination of both 1σ and 3σ isophotal levels.

In Table 6 we compare the inclinations obtained. Equation 3 has a lower threshold of effectiveness depending on the flattening value (q_0) considered. Since Hall et al. (2012) determined the flattening value q_0 in the i -band, in the optical band we obtained inconsistent results for some galaxies in our sample having ellipticity $1 - \varepsilon \geq q_0 = 0.13$. Therefore, in the following we will discuss the inclination calculated considering the galaxy as infinitesimally thin only in the optical band (see relation 1). Excluding particular cases, the inclination computed with the ellipse fitted to the *NIR* 3σ isophotal level has an averaged difference of $\sim 2^\circ$ with respect to the optical inclination, while the inclination from the *NIR* 1σ isophotal level has an averaged difference of $\sim 4^\circ$ and the mean difference with the inclination from the *NUV* emission is $\sim 3^\circ$. Hence, the inclinations computed with the parameters of the ellipse fitted to the *NIR* image at the 3σ isophotal level are the most congruent with the optical inclination, and following Epinat et al. (2010), this may be the best estimation to measure the galaxy inclination.

When computing the inclination, particular cases showing $\Delta i \gtrsim 10^\circ$ with respect to the optical inclination were detected. Inclinations computed with the *NIR* 3σ isophotal level presented four particular cases: CIG 95, 416, 593 and 936, which have a bright central bulge dominating the *NIR* emission. In the case of the *NUV* emission, the particular cases are CIG 201, 416, 906 and 1003, which

have the most extended *UV* haloes and the largest filaments above the disc. In contrast, CIG 936 is the only one particular case obtained for the *NIR* 1σ isophotal level. The galaxy CIG 936 (Figure E12) is an extreme case in our sample displaying its *NIR* and $H\alpha$ emission concentrated in the inner central ~ 30 arcsec (~ 6.3 kpc) of a disc with optical diameter of $D_{25}(B) = 185.4$ arcsec (~ 38.9 kpc). This galaxy might be compared with the Sombrero galaxy (NGC 4594), an S0 galaxy whose bulge governs the axial ratio (e.g. Hall et al. 2012), though we cannot consider CIG 936 an early-type system whilst its disc is dominated by the *UV* emission, tracer of the young stellar population. The results previously described seem to indicate that the apparent discrepancies in the inclination values determined using images in different wavelengths are due to actual asymmetries of the old stellar disc and the presence of an extended *UV* disc and halo.

In conclusion, inclination measurement is essential for unraveling the complex structures of galactic components, in particular *UV* extended discs and haloes. By applying different stellar population tracers, this study allowed us to better separate these different components.

5 RESULTS

In this section we present individual results obtained by comparing properties of the DSS *R*-band, the 2MASS K_s -band, the GALEX *NUV* and *FUV* images versus the $H\alpha$ monochromatic map from FP GHASP data. For each galaxy we indicate the old stellar population disc using the ellipse fitting to the isophotal level at 3σ on the background of the 2MASS K_s -band image, and we trace the young stellar population using both the ellipse corresponding to the $\mu_{NUV,FUV} = 28$ mag arcsec $^{-2}$ and the 1σ isophote of the GALEX *NUV* and *FUV* images. An example is shown in Figure 3.

CIG 71 (UGC 1391): The $H\alpha$ monochromatic map shows a discontinuous disc mainly shifted Southwards from the photometric centre of the *NIR*-band exceeding the radius of the old stellar disc. A prominent and luminous knot is observed at ~ 30 arcsec Southwards from the *NIR* photometric centre. The K_s -band image shows a symmetrical disc within the ellipse fitted to the 3σ brightness level, but the disc becomes more extended and warped towards the South. The *FUV* emission is concentrated near the galactic disc centre and then spreads Southwards at lower brightness. This map also shows a *FUV* emission cloud in the North. The *NUV* emission displays a continuous disc extended along the major axis beyond the old stellar population disc. The photometric centre does not match with the $H\alpha$, *NUV*, and *FUV* emission maxima. The isolation criteria of Verley et al. (2007b) placed CIG 71 outside the isolation plane (see Figure 2), which was confirmed using H I emission by Jones et al. (2018). Moreover, we observed that CIG 71 has common features observed in interacting galaxies (e.g. NGC 5258 from KPG 389, Fuentes-Carrera et al. 2019). Likely, this galaxy experienced an interaction despite its nearest neighbor is 384 kpc away (see Table 2).

Remaining galaxies are discussed in Appendix D.

6 DISCUSSION

In the following we discuss our findings at the light of the current literature focusing on three aspects: the stellar and warm gas emission in the disc, the detection of extraplanar warm gas emission and the extension of the *UV* emission with respect to *NIR* and $H\alpha$ emission.

6.1 The emission in the disc

In this work, we have examined the location of both the old and young stellar population in order to determine the boundaries of the galactic disc in highly inclined galaxies to reveal the existence or lack of a gaseous extraplanar component. Since in late-type galaxies the old and young stellar populations are mixed in the disc and arms, and to be consistent with previous photometric results (see e.g. Jarrett et al. 2003), we normalised the stellar disc using the ellipse fitted to the 3σ on the background level of the *NIR* image, which delimits the region occupied by both old and young stellar populations.

Nonetheless, the definition of the galactic disc, which is used to find an extraplanar component, is not immediately obvious. In Figures 3, and E1 to E13, we plot the DSS *R*-band image of galaxies in our sample to compare images in different wavelengths with the optical one. We observe that the radius of the *R*-band image is larger than the radius of the isophotal 20 mag arcsec $^{-2}$ radius in K_s -band. In fact, Jarrett (2000) compared the K_s -band to optical-band (*B*-band) imaging properties (size, total flux, central surface brightness and elongation) in order to understand the stellar light coming from different components. He found that the *K*-band elliptical isophotal diameter corresponding to $\mu_K = 20$ mag arcsec $^{-2}$ surface brightness (D_{20}) represents about 70% of the optical radius measured at $\mu_B = 25$ mag arcsec $^{-2}$, showing that the *NIR* sensitivity decreases for the later-type (i.e., ‘blue’) galaxies, and concluding that as late-type galaxies evolve, their cores gradually shift towards reddening and brightening, resembling early-type disks or spheroids. Certainly, the K_s -band predominantly traces the oldest stellar population (stars older than ~ 4 Gyr, Fingerhut et al. 2010, and references therein), while optical bands like *R* or *B*-band are more sensitive to the younger, bluer stars. Therefore, it is expected that K_s -band measurements correspond to a smaller region. Since our main goal is to study the extraplanar ionized gas component in edge-on galaxies, we use 2MASS K_s -band imagery looking specifically the location of the old stellar population, tracer of the galactic fundamental structure, with the aim of isolating the oldest stars from the effects of young, blue stars.

On the other hand, the *Wide-field Infrared Survey Explorer* (WISE) have completed a mid-infrared survey of the entire sky in bands centered at wavelengths of 3.4, 4.6, 12, and 22 μm . However, its angular resolution of 6.1 arcsec, 6.4 arcsec, 6.5 arcsec, and 12.0 arcsec at these bands respectively (e.g. Wright et al. 2010; Jarrett et al. 2012), is notably inferior compared to the higher angular resolution of 2.0 arcsec achieved by the 2MASS for the K_s -band images. Therefore, the selection of the narrow-band K_s -band imagery for our analysis offers a clear advantage over the DSS *R*-band or WISE data, as it allows a more precise distinction of the galactic components we are interested in studying in the galaxies in our sample. This choice allows us to discriminate between galactic disc emission and extraplanar emission, providing us with a more solid basis for our analysis and interpretation of the eDIG in galaxies of our sample.

Considering that the mass of our galaxy sample ranges between 10^9 and $10^{10} M_\odot$ (see Table 7), one might infer that our galaxies are dwarf galaxies with fainter emission in older stellar populations. To explore the classification of dwarf galaxies, we compare our sample with the dwarf irregular (dI) galaxies from Fingerhut et al. (2010)’s survey. Firstly, it is worth noting that most of these dI galaxies were too faint to be detected by the 2MASS, implying magnitudes of $K \geq 13.5$ mag (Jarrett et al. 2000; Jarrett 2000; Jarrett et al. 2003). Secondly, the mass range of their dI sample falls between 10^7 to $10^9 M_\odot$ (McCall et al. 2012). In contrast, our sample

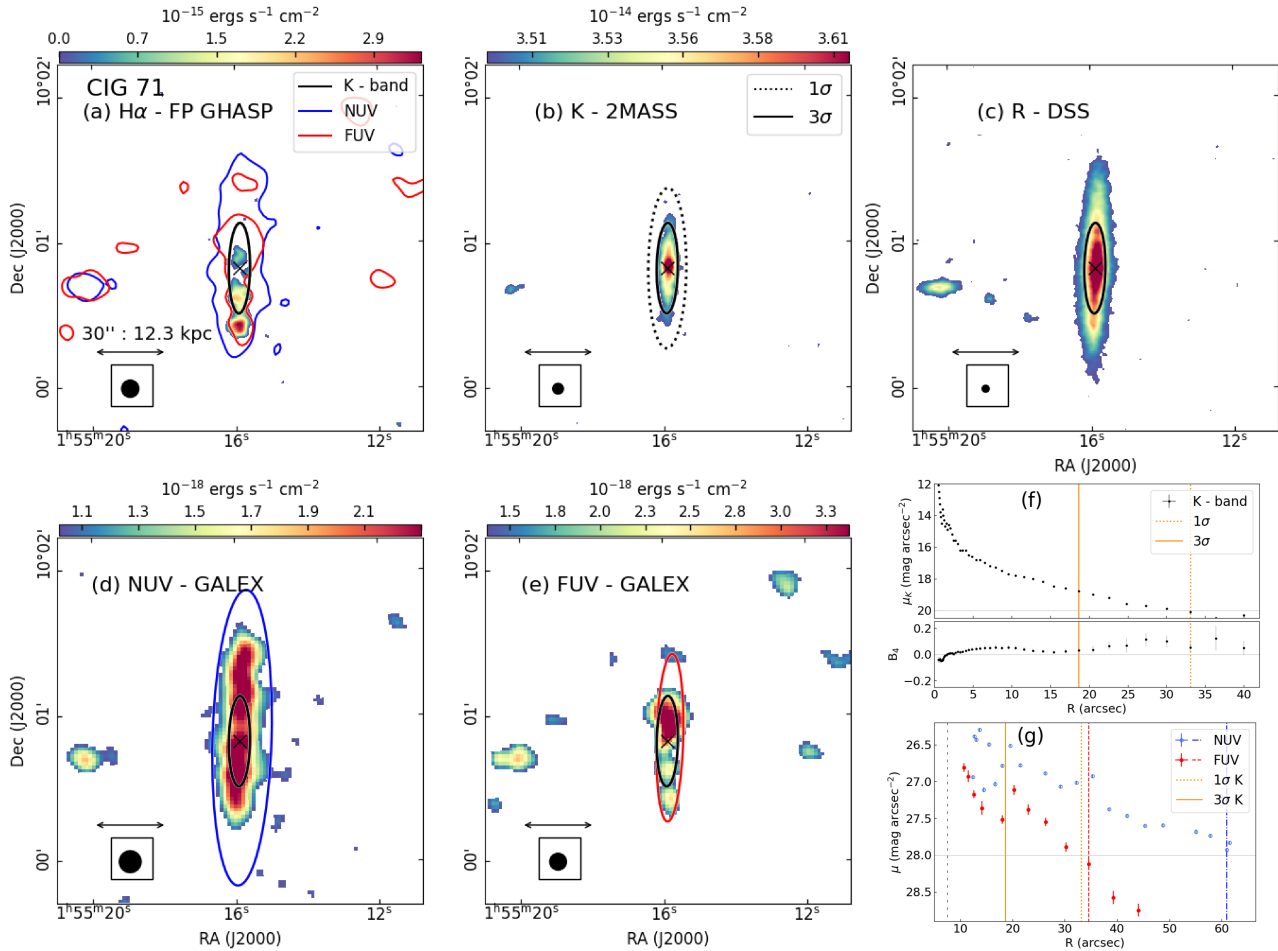


Figure 3. Example of the layout of the graphs and maps of each galaxy. CIG 71 (UGC 1301). Multiwavelength maps of the galaxy: (a) the H α monochromatic map from FP-GHASP data; (b) the 2MASS K_s -band image; (c) the DSS R -band image; (d) and (e) the GALEX NUV and FUV images, respectively. In panels (f) and (g) the surface brightness profile of the K_s -band and NUV/FUV emissions are plotted, respectively. In both panels, yellow vertical lines mark the surface brightness level at 1σ (dotted line) and 3σ (solid line) of the K_s -band image. In panel (g), vertical lines indicate the radii corresponding to the isophotes at a surface brightness level at $\mu_{NUV,FUV} = 28$ mag arcsec $^{-2}$ for the NUV (blue dot-dashed line) and FUV (red dashed line) maps, respectively. Additionally, the vertical black loosely-dashed line at ~ 5 arcsec shows the approximate FWHM of the GALEX point spread function (see e.g. Marino et al. 2010). The ellipses fitted to these isophotes are superimposed on the corresponding map with their associated colour. The common elements in panels (a), (b), (d) and (e) are: a colour-bar indicating the flux in units of erg sec $^{-1}$ cm $^{-2}$, the arrow tracing a scale of 30 arcsec, a black circle embedded in a box indicating the spatial resolution of the image, a black ellipse representing the surface brightness level at 3σ on the background of the K_s -band image and, a black cross (\times) pointing the location of the NIR band peak light distribution. At the bottom of panel (f) we show the relationship between the coefficient B_4 and the radius using the K_s -band map to determine if the isophotes tend to have ‘disc-like’ ($B_4 < 0$) or ‘boxy’ ($B_4 > 0$) shape (see Section 4). Finally, in panel (a), on the H α monochromatic map were overlaid the 1σ isophotes on the background of the NUV and FUV images.

consists of galaxies with apparent K_s -band magnitude $K \leq 13.5$ mag (see selection criteria in Section 2), exhibiting masses one order magnitude higher and having been previously studied in the context of the 2MASS LGA and the 2MASS *Extended Source Catalogue*. This prior analysis ensures that our galaxies are indeed extended objects with bright NIR photometry. Therefore, in the context of Fingerhut et al. (2010), our sample does not align with the category of dwarf galaxies. Since we are not studying dwarf galaxies, we could claim that the surface brightness isophote at 3σ of the K_s -band image, selected to trace the stellar disc, encompasses the light of both the bulge and the disc.

Inside the ellipses fitted to the 3σ level of the $2.22 \mu m$ images, we observed regular discs, while the isophote at 1σ level shows that the old stars at the borders follow the shape of the halo. For instance, the faintest NIR emission in CIG 71 suggests that the old stars are displaced to the South as well as the H α emission, and in CIG 201

the faint old stars trace the same shape of the filamentary structure outlined by the H α and UV emission. Regarding the behaviour of the B_4 parameter versus the major axis relation (see Section 4), in most galaxies the pattern of the curve changes increasing its dispersion from the radial position of the 3σ level. This is more evident in CIG 71, 171, 329, 847 and 936. While a similar break in the UV surface brightness profiles is traced at the radial position of the isophote at 1σ level of the K_s -band image, as observed in CIG 171, 201 and 906. This break in the surface brightness profiles could define the edge of the stellar disc, however, we still rely in our selection because of the better resolution of the 2MASS than the one of the GALEX images (see Section 3). Moreover, for some galaxies as CIG 329, 922 or 1003, if the stellar disc is defined by the the isophote enclosing $\mu_K = 20$ mag arcsec $^{-2}$ (1σ level), they would appear to be dominated by an old stellar disc and no extraplanar gas would have been detected. In this way, besides to the environmental criteria

adopted for selecting a sample, the paradox in selecting the edge of the stellar disc might be another parameter causing discordance in the published results regarding the detection of eDIG.

We have found a variety of morphologies in different wavelengths in galaxies of our sample. With respect to the old stellar population disc, most of the K_s -band images (12 out of 14) showed regular discs with a central bulge and some small filaments along the disc that do not break the stellar disc symmetry in general. Two galaxies showed an asymmetric or perturbed stellar disc: CIG 416 (Figure E7) presenting a tail shape drawn in its K_s -band image, and CIG 593 (Figure E8) with a truncated old stellar disc that follows the morphology of the disturbed and faint $H\alpha$ disc.

On the other hand, the only one galaxy in our sample reliably identified as LINER (Sabater et al. 2012) and whose photometric analysis revealed a coefficient $B_4 < 0$ suggesting a "boxy" bulge is CIG 329 (Figure E6). Although it is difficult to detect a bar in edge-on galaxies, a plausible explanation could be that there is a bar in CIG 329 which may have undergone a vertical bending instability to form this box-shaped bulge. It is well known that two-thirds of star-forming disc galaxies in the local universe are barred (e.g. Eskridge et al. 2000; Whyte et al. 2002; Aguerra et al. 2009; Masters et al. 2011). Numerical simulations of isolated galaxies have shown that a stellar bar can be formed spontaneously (see e.g. Miller et al. 1970; Hohl 1971; Combes & Sanders 1981b; Sellwood & Wilkinson 1993; Athanassoula 2003; Athanassoula et al. 2013; Sellwood 2013; Saha & Elmegreen 2018; Ghosh et al. 2023), but also, that a bar can be formed by a 1:1 prograde flyby interaction and remain several Gyr after the interaction when galaxies are already separated by several Mpc (e.g. Lang et al. 2014). If the stellar bar of CIG 329 was formed by a secular process, why has no bar formed in other galaxies in our sample? It might be that these galaxies are hostile to bar formation or that the bar has been destroyed in the course of their evolutionary pathways. Indeed, the presence of a massive central bulge can suppress the bar instability (e.g., see Saha & Elmegreen 2018; Kataria & Das 2018). Alternatively, bars can be destroyed by a massive central mass concentration and/or inflow of the interstellar gas in the central region (e.g., see Pfenniger & Norman 1990; Shen & Sellwood 2004; Athanassoula et al. 2005; Bournaud et al. 2005; Hozumi & Hernquist 2005; Athanassoula et al. 2013). Furthermore, recent study by Ghosh et al. (2021) revealed that a minor merger can lead to a substantial weakening of bars, and in extreme cases, even a complete destruction of bars in galaxies.

Since most of the galaxies in our sample showed extraplanar material in both UV and $H\alpha$ emission, in the next sections we discuss some general results from the sample in order to understand the origin of the eDIG and UV -haloes detected.

6.2 The eDIG detection

In general, not all edge-on galaxies show detectable eDIG emission, i.e. a gaseous halo above the layer of H II regions associated with the disc. The presence of eDIG in late-type spirals is a direct consequence of SFR in the underlying galactic disc (e.g. Rossa & Dettmar 2000, 2003a). It has been found that the prominence of gaseous haloes correlates with tracers of star formation in the disc, such as the surface density of FIR emission, the SFR determined by $H\alpha$ luminosity, and dust temperatures (e.g. Heald et al. 2006a; Lu et al. 2023). For instance, Rossa & Dettmar (2000) constructed a diagnostic DIG diagram (DDD) that shows the ratio of the flux densities at 60 and 100 μm expressed as S_{60}/S_{100} versus the ratio of the FIR luminosity (L_{FIR}) divided by the optical diameter of the 25th mag arcsec⁻² isophote squared (D_{25}^2), with which they demonstrated that galaxies

suggesting features associated with starburst activity as $S_{60}/S_{100} \geq 0.4$ and $L_{FIR}/D_{25}^2 \approx 1 \times 10^{40} \text{ erg s}^{-1} \text{ kpc}^{-2}$ are candidates to display eDIG layers.

In order to locate our sample in the DDD, we computed the FIR -luminosity using the expression:

$$L_{FIR} = 3.1 \times 10^{39} d^2 [2.58 S_\nu(60) + S_\nu(100)], \quad (4)$$

with $S_\nu(60)$ and $S_\nu(100)$ in Jy (obtained from Lisenfeld et al. (2007) and presented in Table 1) and d the distance to the galaxy in Mpc (Rossa & Dettmar 2003a). The term D_{25}^2 was expressed in kpc².

From our maps, showed in Section 5 and in Appendix E, we detected galaxies showing one or more morphological eDIG features (see e.g. Rossa & Dettmar 2003a; Heald et al. 2006a; Rosado et al. 2013), summarized in Table 7. The brightest H II regions in Local Group galaxies have a surface brightness detection between magnitude orders of 10^{-14} and $10^{-15} \text{ erg s}^{-1} \text{ cm}^2 \text{ arcsec}^{-2}$ (e.g. Hodge & Lee 1990; Azimlu et al. 2011; Cedrés et al. 2012), while the estimated mean sensitivity for the eDIG observed in other galaxies, such as NGC 891 or NGC 4565, is on the order of $10^{-18} \text{ erg s}^{-1} \text{ cm}^2 \text{ arcsec}^{-2}$ (e.g. Rand 1996; Rossa & Dettmar 2003b; Ho et al. 2016; Jones et al. 2017). For this work, the surface brightness detection limit of GHASP is $2.5 \times 10^{-17} \text{ erg s}^{-1} \text{ cm}^2 \text{ arcsec}^{-2}$ (Epinat et al. 2008; Gómez-López et al. 2019; Sardaneta et al. 2022), which is shallower than needed for detection of the faintest eDIG, but still within an acceptable range of sensitivity to offer a reliable perspective for our study.

By discriminating the $H\alpha$ emission in z -direction from the galaxies displaying $H\alpha$ emitting gas extended radially, almost all the galaxies in our sample showed $H\alpha$ emitting gas extended radially outside from the stellar disc, CIG 1003 being the only exception, whose $H\alpha$ emission is concentrated in the central regions drawing a cone shape and ionized gas filaments. In the vertical direction, the $H\alpha$ monochromatic maps display eDIG configurations such as filamentary structures in CIG 71, 329, 593 and 1003; layers of diffuse gas in CIG 201, 329, 416; and patches or detached clouds of ionized gas emission in CIG 95, 159, 593, 922, 847 and 1003. In some cases, the ionized gas falls in the outskirts of the stellar disc tracing a warped structure likely from a recent interaction as in CIG 71 and 183. We have not detected any extraplanar $H\alpha$ emission in the vertical direction in CIG 171, 906 and 936.

As shown in the top left panel of Figure 4, we compare the position in the DDD of our galaxies with those in the Rossa & Dettmar (2003a) sample which contains 62 spiral galaxies with inclination $i > 76^\circ$, an optical diameter of $3 \leq D_{25} \leq 12$ and radial velocity $V_{rad} \leq 6000 \text{ km s}^{-1}$, all of them detected with IRAS in the FIR . We must consider that when defining extraplanar emission, Rossa & Dettmar (2003a) did not distinguish between radially or vertically extended $H\alpha$ emission. In this case, all our galaxies would have eDIG. To ensure a more reliable comparison, in Figure 4, we differentiate between galaxies in our sample with and without vertically extended $H\alpha$ emission.

Figure 4 shows that 6 out of 14 galaxies (42%) of our sample lie above the threshold of warm galaxies at $S_{60}/S_{100} \geq 0.4$ (horizontal dashed line). Half of these galaxies, namely CIG 71, 936 and 1003, are located outside the region of bona fide isolated galaxies of the AMIGA sample (see Figure 2). In this context, we explore the possibility that eDIG incidence is correlated with the environment. In fact, Lisenfeld et al. (2007) found that the value of S_{60}/S_{100} of the AMIGA sample is lower than the one of interacting samples from the literature indicating that the interaction can increase the dust temperature. The panel (a) of Figure 4 also shows that our sample

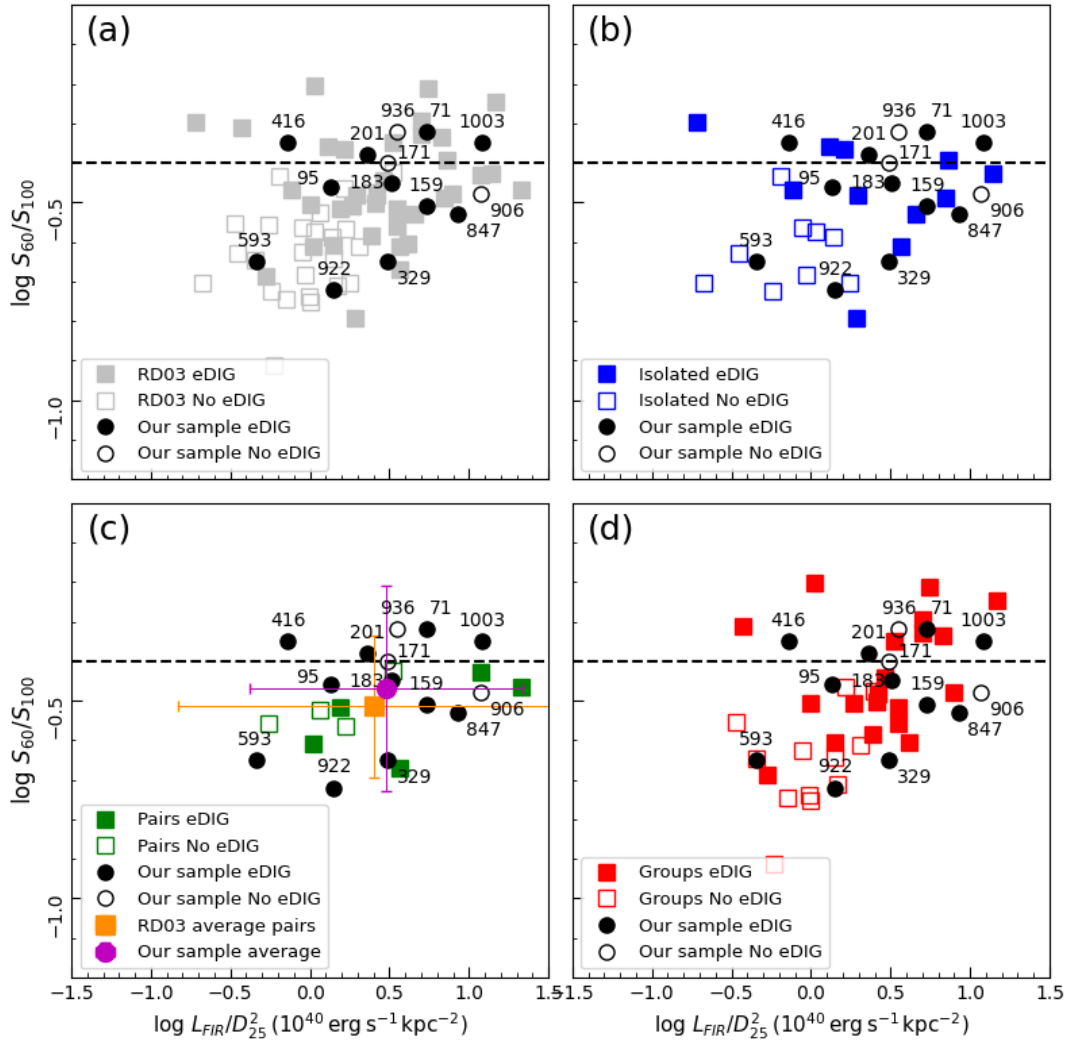


Figure 4. Diagnostic DIG diagram (Rossa & Dettmar 2003a) showing the flux densities ratio at $60\ \mu\text{m}$ and $100\ \mu\text{m}$ (S_{60}/S_{100}) versus the ratio of the FIR luminosity (L_{FIR}) divided by the optical diameter of the 25^{th} mag arcsec^{-1} isophote squared (D_{25}^2) in units of $10^{40}\ \text{ergs s}^{-1}\text{kpc}^{-2}$. The horizontal dashed line marks the threshold for warm galaxies at $S_{60}/S_{100} \geq 0.4$. We compare our sample (black circles with the CIG catalogue numbers indicated) with the whole sample (frame a) of Rossa & Dettmar (2003a) (squares) labelled RD03. Then, we use the hierarchy published in databases to distinguish whether the galaxies in the Rossa & Dettmar (2003a) sample are isolated (frame b), in pairs (frame c) or in groups (frame d) (see Table F1). Due to the low number of galactic pairs in the Rossa & Dettmar (2003a) sample, in panel (c) we also compare the mean values and confidence intervals (see Gehrels 1986) of this subsample (square) and that of our sample (circle). In all panels we distinguish between galaxies that have (filled markers) or do not have eDIG (empty markers).

and the Rossa & Dettmar (2003a) sample share a similar distribution: galaxies with eDIG from both samples populate the entire plane.

Rossa & Dettmar (2003a) rejected galaxies in compact groups but included widely spaced pairs of galaxies. We associated an environmental classification to their sample using NED and Simbad¹⁹ databases, by distinguishing groups, galaxy pairs and relatively isolated galaxies, whereby galaxies with siblings at a distance at $d < 1^\circ$ were included in galaxies belonging to a galactic group and, galaxies with siblings at $d > 1^\circ$ and galaxies with no record were considered isolated (see Table F1). These sub-samples are plotted in the (b), (c) and (d) panels of Figure 4. Rossa & Dettmar (2003a) detected eDIG in 5 out of 9 (56%) paired galaxies and in 21 out of 34 (62%) galaxies in groups: that is, in 26 out of 45 (58%)

interacting galaxies, while, for the sub-sample of isolated galaxies, the eDIG was detected in 10 out of 19 (53%) targets. If we do not distinguish between radial and vertically extended emission, we detected H α emission extended outside the disc in all galaxies in our sample. However, due to the inaccuracies that may exist in the definition of the stellar disc (see Section 4), we consider having detected eDIG only in 11 out of 14 galaxies (79%) where the diffuse ionized gas extends out of the disc vertically.

From the comparison with the entire sample of Rossa & Dettmar (2003a) we suggest that the environment is not connected with the presence of the eDIG. Confirming that the incidence of eDIG in late-type spirals is a direct consequence of the SFR in the underlying galactic disc as found by Rossa & Dettmar (2003a). The interaction could trigger the SFR for a short period of time. However, we also detect eDIG in a high percentage of galaxies that have been isolated for a long period of time.

¹⁹ "The SIMBAD astronomical database", (Wenger et al. 2000).

Table 7. Maximum radial (r) and vertical (z) distance reached by the extra-planar component in UV and $H\alpha$ emission.

CIG Name (1)	<i>MIR</i>	<i>NUV</i>		<i>FUV</i>		$H\alpha$		$H\alpha$	Morphological
	M_* ($10^9 M_\odot$) (2)	z (kpc) (3)	r (kpc) (4)	z (kpc) (5)	r (kpc) (6)	z (kpc) (7)	r (kpc) (8)	eDIG morphology (9)	features (10)
71	14.1	4.2	8.8	2.0	3.9	1.2	4.7	E(r)	A, Ph, UV,
95	3.6	1.8	12.1	1.8	12.1	1.8	10.4	E(r), H II-R	Ph, UV
159	3.8	1.4	10.7	...	1.7	0.5	9.6	E(r), H II-R	W, L($H\alpha$), L(FUV), T
171	1.4	1.9	6.2	...	5.6	...	4.8	E(r), H II-R	A, UV
183	8.1	4.5	8.0	2.6	8.0	2.8	8.0	E(r)(z), H II-R, P	A, W, K, Ph
201	5.1	2.3	10.0	2.3	8.9	1.8	8.7	E(r)(z), P, F	A, K
329	31.8	3.3	8.1	1.8	6.2	1.7	4.1	E(r)(z), F	B, A, UV
416	2.6	1.2	7.1	1.1	6.2	1.0	2.9	E(r)(z), H II-R, F	A, K, UV
593	12.1	2.5	13.0	2.1	11.0	1.6	9.3	H II-R	A, W, UV, L($H\alpha$)
847	11.9	0.9	8.3	1.0	8.6	0.3	4.3	E(r), H II-R	W, K, Ph
906	5.1	3.1	8.0	2.9	8.0	...	1.4	F	Ph, UV, L($H\alpha$)
922	4.3	1.9	9.1	1.5	9.1	1.0	4.5	E(r), H II-R	A, W, UV
936	1.0	1.7	18.4	...	17.7	...	1.4	H II-R	UV, L($H\alpha$), T
1003	6.0	3.2	4.4	1.3	1.2	1.2	...	E(z), F	A, W, K, UV

Columns: (1) CIG galaxy name; (2) Stellar mass (M_*) computed with *Wide-field Infrared Survey Explorer* (WISE) data at *MIR* band (see equation C1); (3) and (4), (5) and (6) and (7) and (8) averaged maximum radial (r) and vertical (z) distance reached by the extra-planar component at *NUV*, *FUV* and $H\alpha$ emission, respectively; (9) morphological description of the extraplanar warm gas component or eDIG; E: extended emission in radial (r - or vertical (z)-direction mostly, P: patches, F: filaments, H II-R: extraplanar H II region; (10) morphological features in different wavelengths: B: bar, A: asymmetric disc, W: warped disc, K: multiple inner emission knots, Ph: unmatched photometric maxima, UV: disc dominated by the UV halo, L(λ): Low emission detected in the wavelength band λ . T: thin disc structure.

6.3 The UV-halo

From the comparison between the $H\alpha$ and the UV imagery, Thilker et al. (2007) discovered that 30% of low inclined galaxies ($i < 80^\circ$) in the local universe present extended UV emission in the extreme outer disc where the number of H II regions expected is negligible with respect to the UV emission regions. In the case of high inclined galaxies ($i > 80^\circ$), extended diffuse UV emission up to 15-20 kpc above the disc midplane has been detected (e.g. Hodges-Kluck & Bregman 2014), which always coincides with the presence of the extraplanar $H\alpha$ emission, although sometimes the ionized gas component is only detected at lower heights (Hodges-Kluck et al. 2016; Jo et al. 2018).

From the individual maps displayed in Figure 3 and Figures E1 to E13, we found that all galaxies in our sample present radial or vertically extended NUV emission, that all galaxies have radially extended FUV emission, and that 11 out of 14 galaxies show vertically extended FUV emission. These 11 galaxies displaying UV halo agree with the galaxies in our sample showing diffuse ionized gas extended out of the disc vertically (eDIG) (see Table 7). We also observed that in most galaxies in our sample presenting the ionized gas extraplanar component, the $H\alpha$ and UV emissions have very similar morphology and the UV halo persists reaching larger heights where the ionized gas is no longer detected, as observed previously by Hoopes et al. (2001) and Hodges-Kluck et al. (2016). And, finally, even in galaxies where we did not observe any extraplanar (z -axis direction) $H\alpha$ emission (CIG 159, 171 and 936), we still have detected an UV halo in the NUV emission.

We found that 7 out of 14 (50%) galaxies of our sample showing a radially extended UV disc presented at least one feature of what could be perceived as a recent interaction such as disturbed ionized gas disc (CIG 71, 95, 171, 183, 416, 593, 847) and/or mismatch of the gaseous and stellar maxima (CIG 71, 95, 183, 593, 847) suggesting that the environment might be a potential cause of these events, even within isolated galaxies. From studies to low-inclined

galaxies, it has been proposed that the extended UV disc might be a consequence of young stars associated with low-mass stellar associations located at large galactocentric distances (Gil de Paz et al. 2007b) which were likely triggered by recent/ongoing interaction events or a high specific rate of gas accretion (Thilker et al. 2007). However, it is assumed that isolated galaxies have not experienced gravitational influences from its close neighbours over the past few billion years (e.g. Karachentseva et al. 2010; Verdes-Montenegro et al. 2005; Rampazzo et al. 2016). Moreover, the lack of signals from a short-term event as a past major merger implies that the mechanism that supplies the gas needed to form the UV extension has been working for a prolonged duration to achieve this level of richness (Thilker et al. 2007). Studying UV photometry of cluster galaxies, Cortese et al. (2012) interpreted the extended UV emission as the result of the consumption of their H I reservoir, inferring that this growth could be stopped and even reversed if the atomic hydrogen is removed via some kind of environmental effect. Therefore, the observed UV extension could potentially be the result of scattering dust particles stemming from ongoing regions of star formation (see e.g. Shinn & Seon 2015), potentially introducing attenuation effects that shape the observed UV emission.

We observed that the UV halo (vertically extended UV emission) in galaxies CIG 201, 329 and 1003 does not trace a structured disc, these haloes are more extensive and have complex filamentary structures that match the $H\alpha$ and *NIR* morphology. Moreover, the *NIR*, $H\alpha$ and UV emission detected in CIG 201 and 1003 shows signs of a cone-shape suggesting the presence of a central outflow (see individual galaxy notes in the Appendix D). From the comparison between UV and *NIR* imagery, it has been shown that UV halo along the major axis relative to the optical radius R_{25} is unrelated to the prominence of the bulge and, therefore, the radially concentrated UV haloes are unlikely light from the bulge outskirts (Hodges-Kluck et al. 2016). In the case of CIG 201, 329 and 1003, the UV diffuse emission might be expected as a result of scattered UV light that escape from

the disc dust (Diffuse extraplanar Dust, eDust) or emission from hot core-helium-burning stars (Hoopes et al. 2005). The simultaneity between the eDust and the extraplanar H α emission suggests that a large fraction of the H α emission could be originated from the galactic plane and is scattered by the eDust into the galactic halo (Hoopes et al. 2005; Seon et al. 2011; Jo et al. 2018).

On the other hand, the existence of an UV halo does not always mean the existence of eDust (e.g. Shinn 2019). We observed that in 10 out of 14 galaxies (71%) of our sample presenting an UV halo (CIG 71, 95, 159, 171, 183, 416, 593, 847, 906, 922), the UV light reveals an intense brightness and a vertical extension above the galactic centre, which gradually decreases with increasing distance from the galactic centre, rather indicating a disc extended structure. Other possible mechanisms producers of diffuse-and-global UV haloes are galactic radiation, (magneto-)hydrodynamic phenomena or accretion from the CGM or ICM (Hodges-Kluck & Bregman 2014; Shinn & Seon 2015; Hodges-Kluck et al. 2016; Shinn 2019). Conversely, Hodges-Kluck et al. (2016) observed that the UV haloes are brightest over the parts of the disc with bright H α , X-ray, or radio emission, suggesting that they are connected to star formation in the disc, but not necessarily in a way that requires ionizing photons or winds to escape the disc.

Previous studies about the origin of the eDIG have found regions consistent with mixed OB and hot low-mass evolved stars (HOLMES), and OB–shock ionization as the primary driver of eDIG ionization (Flores-Fajardo et al. 2011; Jones et al. 2017; Levy et al. 2019; Rautio et al. 2022). The NUV light is dominated by stars in the turn-off point in the HR-diagram (turn-off stars), while, the FUV emission of old ‘normal’ stellar populations is dominated by post asymptotic giant branch (PAGB) stars (e.g. Marino et al. 2011b). HOLMES, which include PAGB stars and white dwarfs, are found abundantly in the thick discs and lower haloes of galaxies. Their considerable vertical distribution compared to OB stars and their significant contribution to the UV radiation of galaxies (see e.g. Rautio et al. 2022, and references therein), make them candidates to be a source of eDIG ionization and, consequently, of UV haloes.

However, while late-type galaxies in nearby groups, observed from various inclination angles (ranging from 58° to 90°), display FUV and NUV images practically identical (e.g. Marino et al. 2010), our isolated galaxies, as previously noted in early-type galaxies, reveal that the FUV emission appears more compact and luminous compared to the NUV emission (e.g. Gil de Paz et al. 2007a; Rampazzo et al. 2007; Jeong et al. 2007; Marino et al. 2010, 2011a,b). Following Cortese et al. (2012), if the extended UV emission arises from the conversion of atomic hydrogen gas into new stars, it suggests that the stellar population is becoming younger or more metal-poor. As a result, the turn-off stars shift to bluer colours and higher luminosity, increasing the NUV emission. Simultaneously, the contribution to the FUV from PAGB stars decrease because, despite their higher luminosity, the duration of the PAGB phase gets much shorter due to decreased available fuel (Marino et al. 2011b).

In summary, the nature of UV haloes in galaxies are subject to a complex interplay of factors, including SF, ionization processes, and possible CGM or ICM contributions. Further investigation of the specific mechanisms driving UV haloes is needed to fully understand their origin and importance in different galactic environments.

7 SUMMARY AND CONCLUSIONS

Isolated galaxies constitute a reference model to study the environmental influence on galaxy evolution. In this work we studied

the environmental impact on the incidence of eDIG in a sample of 14 nearby ($z \leq 0.02$) isolated late-type edge-on ($i \geq 80^\circ$) galaxies from the Catalogue of Isolated Galaxies (CIG, Karachentseva 1973). We presented the H α emission maps of galaxies in our sample with data obtained from the scanning Fabry-Perot interferometer, GHASP, offering a complete two-dimensional coverage of the emitting line region. We aimed to determine the galactic plane and to examine the distribution of the warm gaseous component with respect to the old and young stellar populations. Thus, we compared monochromatic H α images with the NIR 2MASS K_s -band and UV from GALEX archive images.

We started by defining the stellar disc using the ellipse fitted to the 3σ on the background level of the 2MASS K_s -band image, which delimits the region occupied by both old and young stellar populations. However, we are aware of selecting the boundary of the stellar disc might be another parameter causing discordance in the published results regarding the detection of eDIG. Thus, we consider having detected eDIG only in the 11 out of 14 galaxies (79%) where the diffuse ionized gas extends out of the disc vertically. If we do not distinguish between radial and vertically extended emission, we would have detected H α emission extended outside the disc in all galaxies in our sample. In this case, we demonstrated that our sample is comparable to the broader sample studied by Rossa & Dettmar (2003a) when studying the incidence of eDIG.

We found that all galaxies in our sample present extraplanar NUV emission in both radial and vertical directions. While 11 out of 14 galaxies (79%) have vertically extended FUV emission, the same galaxies presenting eDIG. Because we showed that at least 79% ($\sim 2/3$) of isolated late-type, high inclined galaxies have both extended UV discs and UV haloes, our study reinforces the observations made by Thilker et al. (2007) who found that one-third of the low-inclined galaxies in the local Universe have extended UV discs. Hence, suggesting that the oldest star formation occurring between ~ 10 and 100 Myrs extends well beyond the disc defined by the H α map which only traces the most recent star formation (younger than 10 Myrs).

We find that the PA obtained with NIR, optical and NUV images varies on average $\Delta PA \approx \pm 2.5^\circ$, which is expected for galaxies that have not experienced strong interactions in the last billions of years. However, when computing the inclination, some cases showed $\Delta i \approx \pm 10^\circ$ with respect to the optical inclination as a consequence of the presence of old stellar population centralized discs and UV extended discs and haloes.

Our study suggests that the eDIG is revealed in a significant fraction of galaxies (79% of the galaxies presented H α emission vertically extended) which have been isolated from a long period of time. When compared with the generic sample of highly inclined galaxies by Rossa & Dettmar (2003a) we did not find evidence that the environment plays a role in the presence of the eDIG incidence. This confirms that the presence of eDIG in late-type spirals is a direct consequence of the SFR in the underlying galactic disc as suggested by Rossa & Dettmar (2003a).

We foresee to discuss the H α kinematics of the galaxies in our sample in a forthcoming paper. Furthermore, since GALEX images are quite faint we are acquiring Astrosat-UVIT (Tandon et al. 2017) pointed observations of our galaxies in the FUV band.

ACKNOWLEDGEMENTS

Based on observations taken with the GHASP spectrograph at the Observatoire de Haute Provence (OHP, France), operated

by the French CNRS. The authors acknowledge the technical assistance provided by the late Olivier Boissin † from LAM and the OHP team before and during the observations, namely the night team: Jean Balcaen, Stéphane Favard, Jean-Pierre Troncin, Didier Gravallon and the day team led by François Moreau. This research has made use of the NASA/IPAC Extragalactic Database (NED), which is operated by the Jet Propulsion Laboratory, California Institute of Technology, under contract with the National Aeronautics and Space Administration. This research has made use of the SIMBAD database, operated at CDS, Strasbourg, France. M.M.S. thanks the “Programa de Becas Posdoctorales en la UNAM” of DGAPA-UNAM. M.R. acknowledges the project CONACyT CF-86367. I.F.C. acknowledges the financial support of SIP-IPN grant no. 20232054.

DATA AVAILABILITY

The data used in this work can be found online on the data servers of *The STScI Digitized Sky Survey*²⁰, *Two Micron All Sky Survey (2MASS)*²¹ and the *Galaxy Evolution Explorer (GALEX)*²². The FP data underlying this article will be shared on reasonable request to the corresponding author.

REFERENCES

- Aguerri J. A. L., Méndez-Abreu J., Corsini E. M., 2009, *A&A*, **495**, A41
- Argudo-Fernández M., et al., 2013, *A&A*, **560**, A9
- Argudo-Fernández M., et al., 2015, *A&A*, **578**, A110
- Athanassoula E., 2003, *MNRAS*, **341**, 1179
- Athanassoula E., Lambert J. C., Dehnen W., 2005, *MNRAS*, **363**, 496
- Athanassoula E., Machado R. E. G., Rodionov S. A., 2013, *MNRAS*, **429**, 1949
- Azimlu M., Marciniak R., Barmby P., 2011, *AJ*, **142**, 139
- Barbosa C. E., et al., 2015, *MNRAS*, **453**, 2965
- Bianchi L., 2011, *Ap&SS*, **335**, 51
- Bizyaev D., et al., 2017, *ApJ*, **839**, 87
- Bizyaev D., Walterbos R. A. M., Chen Y.-M., Drory N., Lane R. R., Brownstein J. R., Riffel R. A., 2022, *MNRAS*, **515**, 1598
- Boselli A., et al., 2010, *PASP*, **122**, 261
- Boselli A., Fossati M., Gavazzi G., Ciesla L., Buat V., Boissier S., Hughes T. M., 2015, *A&A*, **579**, A102
- Boselli A., Fossati M., Ferrarese L., Boissier S., 2018, *A&A*, **614**, A56
- Boselli A., Fossati M., Sun M., 2022, *A&ARv*, **30**, 3
- Bournaud F., Combes F., Semelin B., 2005, *MNRAS*, **364**, L18
- Bradley L., et al., 2020, *astropy/photutils*: 1.0.0, doi:10.5281/zenodo.4044744, <https://doi.org/10.5281/zenodo.4044744>
- Burstein D., 1979, *ApJ*, **234**, 829
- Buta R. J., et al., 2019, *MNRAS*, **488**, 2175
- Cappellari M., Copin Y., 2003, *MNRAS*, **342**, 345
- Cedrés B., Cepa J., Bongiovanni Á., Castañeda H., Sánchez-Portal M., Tomita A., 2012, *A&A*, **545**, A43
- Cluver M. E., et al., 2014, *The Astrophysical Journal*, **782**, 90
- Combes F., Sanders R. H., 1981a, *A&A*, **96**, 164
- Combes F., Sanders R. H., 1981b, *A&A*, **96**, 164
- Cortese L., et al., 2012, *A&A*, **544**, A101
- Daigle O., Carignan C., Amram P., Hernandez O., Chemin L., Balkowski C., Kennicutt R., 2006a, *MNRAS*, **367**, 469
- Daigle O., Carignan C., Hernandez O., Chemin L., Amram P., 2006b, *MNRAS*, **368**, 1016
- Epinat B., Amram P., Marcelin M., 2008, *MNRAS*, **390**, 466
- Epinat B., Amram P., Balkowski C., Marcelin M., 2010, *MNRAS*, **401**, 2113
- Eskridge P. B., et al., 2000, *AJ*, **119**, 536
- Eskridge P. B., et al., 2002, *ApJS*, **143**, 73
- Fingerhut R. L., et al., 2010, *ApJ*, **716**, 792
- Flores-Fajardo N., Morisset C., Stasińska G., Binette L., 2011, *MNRAS*, **415**, 2182
- Fraternali F., Binney J. J., 2006, *MNRAS*, **366**, 449
- Fuentes-Carrera I., et al., 2019, *A&A*, **621**, A25
- Gach J.-L., et al., 2002, *PASP*, **114**, 1043
- Gehrels N., 1986, *ApJ*, **303**, 336
- Ghosh S., Saha K., Di Matteo P., Combes F., 2021, *MNRAS*, **502**, 3085
- Ghosh S., Fragkoudi F., Di Matteo P., Saha K., 2023, *A&A*, **674**, A128
- Gil de Paz A., et al., 2005, *ApJ*, **627**, L29
- Gil de Paz A., et al., 2007a, *ApJS*, **173**, 185
- Gil de Paz A., et al., 2007b, *ApJ*, **661**, 115
- Gómez-López J. A., et al., 2019, *A&A*, **631**, A71
- Gooch R., 1996, in Jacoby G. H., Barnes J., eds, *Astronomical Society of the Pacific Conference Series Vol. 101, Astronomical Data Analysis Software and Systems V*. p. 80
- Hall M., Courteau S., Dutton A. A., McDonald M., Zhu Y., 2012, *MNRAS*, **425**, 2741
- Haynes M. P., Giovanelli R., 1984, *AJ*, **89**, 758
- Heald G. H., Rand R. J., Benjamin R. A., Collins J. A., Bland-Hawthorn J., 2006a, *ApJ*, **636**, 181
- Heald G. H., Rand R. J., Benjamin R. A., Bershadsky M. A., 2006b, *ApJ*, **647**, 1018
- Heald G. H., Rand R. J., Benjamin R. A., Bershadsky M. A., 2007, *ApJ*, **663**, 933
- Ho I. T., et al., 2016, *MNRAS*, **457**, 1257
- Hodge P., Lee M. G., 1990, *PASP*, **102**, 26
- Hodges-Kluck E., Bregman J. N., 2014, *ApJ*, **789**, 131
- Hodges-Kluck E., Cafmeyer J., Bregman J. N., 2016, *ApJ*, **833**, 58
- Hohl F., 1971, *ApJ*, **168**, 343
- Hoopes C. G., Walterbos R. A. M., Bothun G. D., 2001, *ApJ*, **559**, 878
- Hoopes C. G., et al., 2005, *ApJ*, **619**, L99
- Hozumi S., Hernquist L., 2005, *PASJ*, **57**, 719
- HyperLEDA 2016, Makarov, Dmitry and P. Prugniel and N. Terekhova and H. Courtois and I. Vauglin, <http://leda.univ-lyon1.fr/>
- Jarrett T. H., 2000, *PASP*, **112**, 1008
- Jarrett T. H., Chester T., Cutri R., Schneider S., Skrutskie M., Huchra J. P., 2000, *AJ*, **119**, 2498
- Jarrett T. H., Chester T., Cutri R., Schneider S. E., Huchra J. P., 2003, *AJ*, **125**, 525
- Jarrett T. H., et al., 2012, *AJ*, **144**, 68
- Jedrzejewski R. I., 1987, *MNRAS*, **226**, 747
- Jeong H., Bureau M., Yi S. K., Krajnović D., Davies R. L., 2007, *MNRAS*, **376**, 1021
- Jeong H., et al., 2009, *MNRAS*, **398**, 2028
- Jo Y.-S., Seon K.-i., Shinn J.-H., Yang Y., Lee D., Min K.-W., 2018, *ApJ*, **862**, 25
- Jones A., et al., 2017, *A&A*, **599**, A141
- Jones M. G., et al., 2018, *A&A*, **609**, A17
- Joye W. A., Mandel E., 2003, in Payne H. E., Jedrzejewski R. I., Hook R. N., eds, *Astronomical Society of the Pacific Conference Series Vol. 295, Astronomical Data Analysis Software and Systems XII*. p. 489
- Kamphuis P., Peletier R. F., Dettmar R. J., van der Hulst J. M., van der Kruit P. C., Allen R. J., 2007, *A&A*, **468**, 951
- Karachentsev I. D., Makarov D. I., Karachentseva V. E., Melnyk O. V., 2011, *Astrophysical Bulletin*, **66**, 1
- Karachentseva V. E., 1973, *Soobshcheniya Spetsial'noj Astrofizicheskoy Observatorii*, **8**
- Karachentseva V. E., Mitronova S. N., Melnyk O. V., Karachentsev I. D., 2010, *Astrophysical Bulletin*, **65**, 1

²⁰ *The STScI Digitized Sky Survey* https://archive.stsci.edu/cgi-bin/dss_form

²¹ *Two Micron All Sky Survey (2MASS)* <https://irsa.ipac.caltech.edu/Missions/2mass.html>

²² *Galaxy Evolution Explorer (GALEX)* <https://archive.stsci.edu/missions-and-data/galex>

- Kataria S. K., Das M., 2018, *MNRAS*, **475**, 1653
- Kennicutt R. C., Evans N. J., 2012, *ARA&A*, **50**, 531
- Kim T., Athanassoula E., Sheth K., Bosma A., Park M.-G., Lee Y. H., Ann H. B., 2021, *ApJ*, **922**, 196
- Kormendy J., Illingworth G., 1982, *ApJ*, **256**, 460
- Korsaga M., Epinat B., Amram P., Carignan C., Adamczyk P., Sorgho A., 2019, *MNRAS*, **490**, 2977
- Kourkchi E., Tully R. B., Neill J. D., Seibert M., Courtois H. M., Dupuy A., 2019, *ApJ*, **884**, 82
- Lang M., Holley-Bockelmann K., Sinha M., 2014, *ApJ*, **790**, L33
- Levy R. C., et al., 2019, *ApJ*, **882**, 84
- Lisenfeld U., et al., 2007, *A&A*, **462**, 507
- Lu L.-Y., et al., 2023, *MNRAS*, **519**, 6098
- Marino A., Bianchi L., Rampazzo R., Buson L. M., Bettoni D., 2010, *A&A*, **511**, A29
- Marino A., Bianchi L., Rampazzo R., Thilker D., Annibali F., Bressan A., Buson L. M., 2011a, *Ap&SS*, **335**, 243
- Marino A., et al., 2011b, *MNRAS*, **411**, 311
- Masters K. L., et al., 2011, *MNRAS*, **411**, 2026
- McCall M. L., Vaduvescu O., Pozo Nunez F., Barr Dominguez A., Fingerhut R., Unda-Sanzana E., Li B., Albrecht M., 2012, *A&A*, **540**, A49
- Miller S. T., Veilleux S., 2003, *ApJS*, **148**, 383
- Miller R. H., Prendergast K. H., Quirk W. J., 1970, *ApJ*, **161**, 903
- Nersesian A., et al., 2019, *A&A*, **624**, A80
- Peters S. P. C., van der Kruit P. C., Allen R. J., Freeman K. C., 2017, *MNRAS*, **464**, 65
- Pfenniger D., Norman C., 1990, *ApJ*, **363**, 391
- Putman M. E., 2017, in Fox A., Davé R., eds, *Astrophysics and Space Science Library Vol. 430, Gas Accretion onto Galaxies*. p. 1 ([arXiv:1612.00461](https://arxiv.org/abs/1612.00461)), doi:10.1007/978-3-319-52512-9_1
- Putman M. E., Peek J. E. G., Joung M. R., 2012, *ARA&A*, **50**, 491
- Rampazzo R., et al., 2007, *MNRAS*, **381**, 245
- Rampazzo R., et al., 2016, in D’Onofrio M., Rampazzo R., Zaggia S., eds, *Astrophysics and Space Science Library Vol. 435, From the Realm of the Nebulae to Populations of Galaxies*. p. 381, doi:10.1007/978-3-319-31006-0_5
- Rampazzo R., Omizzolo A., Uslenghi M., Román J., Mazzei P., Verdes-Montenegro L., Marino A., Jones M. G., 2020, *A&A*, **640**, A38
- Rand R. J., 1996, *ApJ*, **462**, 712
- Rand R. J., 1998, *Publ. Astron. Soc. Australia*, **15**, 106
- Rautio R. P. V., Watkins A. E., Comerón S., Salo H., Díaz-García S., Janz J., 2022, *A&A*, **659**, A153
- Rosado M., Gabbasov R. F., Repetto P., Fuentes-Carrera I., Amram P., Martos M., Hernandez O., 2013, *AJ*, **145**, 135
- Rossa J., Dettmar R.-J., 2000, *A&A*, **359**, 433
- Rossa J., Dettmar R.-J., 2003a, *A&A*, **406**, 493
- Rossa J., Dettmar R.-J., 2003b, *A&A*, **406**, 505
- Sabater J., Verdes-Montenegro L., Leon S., Best P., Sulentic J., 2012, *A&A*, **545**, A15
- Saha K., Elmegreen B., 2018, *ApJ*, **858**, 24
- Sardaneta M. M., et al., 2022, *A&A*, **659**, A45
- Sellwood J. A., 2013, *Dynamics of Disks and Warps*. Springer Netherlands, Dordrecht, pp 923–983, doi:10.1007/978-94-007-5612-0_18
- Sellwood J. A., Wilkinson A., 1993, *Reports on Progress in Physics*, **56**, 173
- Seon K.-I., Witt A., Kim I.-J., Shinn J.-H., Edelman J., Min K.-W., Han W., 2011, *ApJ*, **743**, 188
- Shen J., Sellwood J. A., 2004, *ApJ*, **604**, 614
- Shinn J.-H., 2019, *MNRAS*, **489**, 4690
- Shinn J.-H., Seon K.-I., 2015, *ApJ*, **815**, 133
- Stone C., Courteau S., Arora N., 2021, *ApJ*, **912**, 41
- Tandon S. N., et al., 2017, *AJ*, **154**, 128
- Thilker D. A., Walterbos R. A. M., Braun R., Hoopes C. G., 2002, *AJ*, **124**, 3118
- Thilker D. A., et al., 2005, *ApJ*, **619**, L79
- Thilker D. A., et al., 2007, *ApJS*, **173**, 538
- Tomičić N., et al., 2021, *ApJ*, **922**, 131
- Verdes-Montenegro L., Sulentic J., Lisenfeld U., Leon S., Espada D., Garcia E., Sabater J., Verley S., 2005, *A&A*, **436**, 443
- Verley S., et al., 2007a, *A&A*, **470**, 505
- Verley S., et al., 2007b, *A&A*, **472**, 121
- Walker I. R., Mihos J. C., Hernquist L., 1996, *ApJ*, **460**, 121
- Wenger M., et al., 2000, *A&AS*, **143**, 9
- Whyte L. F., Abraham R. G., Merrifield M. R., Eskridge P. B., Frogel J. A., Pogge R. W., 2002, *MNRAS*, **336**, 1281
- Wright E. L., et al., 2010, *AJ*, **140**, 1868
- Zschaechner L. K., Rand R. J., Walterbos R., 2015, *ApJ*, **799**, 61
- Zwicky F., Herzog E., Wild P., 1968, *Catalogue of galaxies and of clusters of galaxies*

APPENDIX A: SPATIAL SIGNAL ENHANCEMENT

To enhance the spatial signal-to-noise ratio (SNR), we employed two techniques on the wavelength data cubes. Firstly, we implemented adaptive spatial binning through Voronoi tessellation (Cappellari & Copin 2003; Daigle et al. 2006b,a), aiming for a target SNR of approximately 5 or 7. Additionally, we applied a Gaussian smoothing with a FWHM $\approx 2''$ (3 pix). To maintain a SNR threshold above 5 in the Gaussian smoothed data cube, we performed a comparison between both $H\alpha$ monochromatic maps and we set a limit for the detected emission in the Gaussian smoothed maps. Since we aim to study the morphology of the eDIG, traced by the $H\alpha$ line emission, we opted to utilize the $H\alpha$ monochromatic map resulting from Gaussian smoothing. This map yields a more comprehensive representation of the morphology of the detected $H\alpha$ emitting gas, in comparison to the map obtained through spatial binning via Voronoi tessellation. To illustrate this technique, Figure A1 presents the $H\alpha$ monochromatic map for CIG 847 (UGC 11132).

APPENDIX B: CALIBRATION OF THE TOTAL $H\alpha$ FLUX

As indicated by Epinat et al. (2008), our major scientific goal is not to use the Fabry–Perot technique to make photometric studies but kinematic ones. Therefore, during the observations, we decided not to calibrate our data, saving observing time. On the other hand, there is no $H\alpha$ calibrated images of galaxies in our sample in the literature yet to compare our targets which would provide us with a more accurate flux range. However, to obtain the total $H\alpha$ flux of our galaxies, we can follow previous total $H\alpha$ flux indirect calibrations made by Epinat et al. (2008) and by Gómez-López et al. (2019) for large galaxy samples observed with the same instrument, GHASP.

Epinat et al. (2008) calibrated the total $H\alpha$ flux of more than 200 galaxies from the GHASP sample by making a linear regression of the comparison between monochromatic FP images of 69 galaxies and images with calibrated fluxes from narrow-band filters including $H\alpha$ and [N II] which had been already published. The coefficient of the resulting line is $0.48 \pm 0.06 \times 10^{-16} \text{ W m}^{-2} \text{ ph}^{-1} \text{ s}$, the fitting was forced to pass through the origin for obvious physical reasons. Later, Gómez-López et al. (2019) studied the kinematics of a sample of 152 late-type galaxies from the HRS catalogue²³. In this context, they calibrated indirectly the FP monochromatic $H\alpha$ maps, this time using the calibrated fluxes from Boselli et al. (2015), obtaining a similar coefficient of the resulting line fitted and a GHASP surface brightness detection limits of $\sim 2.5 \pm 0.2 \times 10^{-17} \text{ ergs s}^{-1} \text{ cm}^{-2} \text{ arcsec}^{-2}$ for 2 hours exposure time, resulting in objects with an average lower threshold of $\text{SNR} \geq 5$. This value of surface brightness detection limit was also obtained by Sardaneta et al. (2022) when, studying the

²³ *The Herschel Reference survey* (HRS; Boselli et al. 2010)

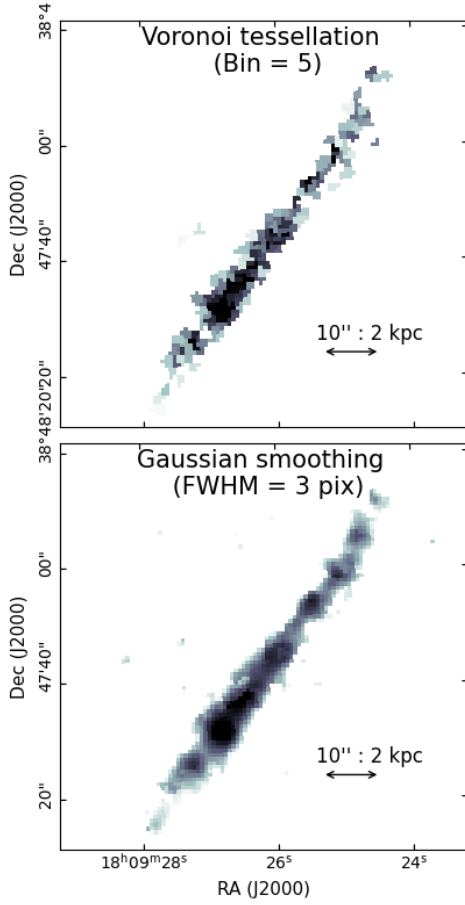


Figure A1. $H\alpha$ monochromatic map of CIG 847 (UGC 11132) obtained after being applied a Voronoi tessellation (VT) with signal-to-noise ratio $\text{SNR} \approx 5$ (top panel) and a spatial Gaussian smoothing with $\text{FWHM} \approx 2''$ (3 pix) (bottom panel). We use the VT binned map to mask the Gaussian smoothed map to ensure that all regions of this map have $\text{SNR} \geq 5$.

kinematics of the eDIG in the ram-pressure stripped Virgo galaxy NGC 4330, compared the GHASP $H\alpha$ monochromatic image of this galaxy with the deep CFHT $H\alpha$ image from VESTIGE survey²⁴.

Thus, from the results obtained for galaxies observed with the FP GHASP, we estimated the integrated flux of each galaxy in the sample studied in this work. We list these integrated fluxes in Table B1.

APPENDIX C: STELLAR MASS FROM MIR

Wide-field Infrared Survey Explorer (WISE) is a NASA-funded Medium-Class Explorer mission that consists of a 40 cm space infrared telescope, whose science instrumentation includes 1024×1024 pixel² arrays of Si:As and HgCdTe. WISE mapped the entire sky at $3.4 \mu\text{m}$ (W_1), $4.6 \mu\text{m}$ (W_2), $12 \mu\text{m}$ (W_3), and $22 \mu\text{m}$ (W_4). Each band covers a field-of-view of 47×47 arcmin² with an angular resolution of 6.0 arcsec in the short band-pass and 12.0 arcsec in the longest one and a 1.375 arcsec pixel scale (Jarrett et al. 2012). We infer the stellar mass using the mass-to-light (M/L) ratio of galaxies

²⁴ A *Virgo Environmental Survey Tracing Ionised Gas Emission* (VESTIGE; Boselli et al. 2018)

Table B1. $H\alpha$ integrated fluxes deduced from previous extrapolations to large galaxy surveys observed with GHASP (see e.g. Epinat et al. 2008; Gómez-López et al. 2019)

CIG Name	Flux		
	(ph s^{-1})	($10^{-16} \text{ W m}^{-2}$)	($10^{-15} \text{ erg s}^{-1} \text{ cm}^{-2}$)
71	0.61	0.29	2.93
95	0.30	0.14	1.42
159	0.42	0.20	2.03
171	0.34	0.16	1.64
183	0.44	0.21	2.14
201	1.80	0.86	8.62
329	0.83	0.40	3.97
416	0.36	0.17	1.74
593	0.06	0.03	0.28
847	0.19	0.09	0.93
906	0.20	0.10	0.96
922	0.36	0.17	1.74
936	0.19	0.09	0.93
1003	0.26	0.12	1.23

Table C1. Stellar mass and luminosity computed with the mid- and far-infrared magnitudes respectively.

CIG Name	W_1 ($3.4 \mu\text{m}$) (mag)	W_2 ($4.6 \mu\text{m}$) (mag)	M_* ($10^{10} M_\odot$)
(1)	(2)	(3)	(4)
71	11.42	11.32	1.41
95	12.59	12.53	0.36
159	11.06	10.93	0.38
171	11.58	11.18	0.14
183	11.99	12.01	0.81
201	11.10	11.01	0.51
329	10.46	10.53	3.18
416	12.40	12.28	0.26
593	11.44	11.48	1.21
847	11.28	11.18	1.19
906	10.83	10.58	0.51
922	12.03	11.95	0.43
936	11.57	11.36	0.10
1003	11.00	10.75	0.60

Columns: (1) CIG galaxy name; (2) and (3) *Wide-field Infrared Survey Explorer* (WISE) 3.4 and $4.6 \mu\text{m}$ colour, respectively; (4) stellar mass computed using the relation C1.

(e.g. Korsaga et al. 2019). For low- z galaxies, the stellar M/L has a linear trend with WISE W_1 ($3.4 \mu\text{m}$) – W_2 ($4.6 \mu\text{m}$) colour (Cluver et al. 2014):

$$\log(M_*/L_{W_1}) = -2.54(W_1 - W_2) - 0.17, \quad (\text{C1})$$

with $L_{W_1}(L_\odot) = 10^{-0.4(M - M_\odot)}$, where M is the absolute magnitude of the source in W_1 , $M_\odot = 3.24$ mag, and $W_1 - W_2$ is the rest-frame colour of the source. Mid-infrared magnitudes and stellar masses are listed in Table C1.

APPENDIX D: INDIVIDUAL GALAXIES

We provide the individual notes as discussed in Section 5.

CIG 95 (UGC 1733). Figure E1: The $H\alpha$ map shows a detached cloud from the disc that exceeds radially the old stellar population disc observed in the NIR -band emission. The brightest $H\alpha$ emission region is much wider than the old stellar disc and exceeds it in the z -direction. The $2.22\mu\text{m}$ image reveals a central bulge surrounded by an asymmetric warped old stellar population disc that extends Southward. The FUV emission displays an extended and warped disc. The NUV emission traces a well-bound large disc with a brighter Southeastern tip and a sharpened, fainter Northwestern tip. The $H\alpha$, FUV and NUV emissions match in maxima emission but it is located to the Southeastern edge of the old stellar population disc. From the SDSS optical images, Buta et al. (2019) defined CIG 95 as a Sc warped (see Table 1). Although the galaxy appears to be slightly pulled to the Southeast, indicating a possible interaction, CIG 95 meets all the isolation criteria of the AMIGA sample (see Section 2).

CIG 159 (UGC 3326). Figure E2: The $H\alpha$ emission displays a discontinuous disc composed of bright clouds uniformly distributed along the major axis with a size similar to that of the K_s -band 1σ isophote. The K_s -band image of the galaxy shows a large thin warped disc with a central bulge. The GALEX FUV image shows a few faint clouds mostly at the photometric centre. The NUV emission draws a warped disc brighter on the East side than on the West side. The GALEX NUV and FUV images have low SNR which may yield spurious surface brightness profiles. The location of the $H\alpha$ emission is consistent with the NUV emission. The emission maxima of the four emissions presented in Figure E2 coincide within ~ 5 arcsec. Further spectral data and deeper, higher resolution UV images are required to draw a conclusion about the morphology of this apparently quiescent galaxy. However, Jones et al. (2018) found that in the $H\text{ I}$ emission CIG 159 is a not an isolated galaxy

CIG 171 (UGC 3474). Figure E3: The $H\alpha$ emission is brighter in the South than the North likely shadowed by dust and stars emitting in UV. In the South the ionized gas has a dense distribution while in the North it traces detached clouds. The old stellar population disc is mostly symmetric with feathering along the edges. The NUV and FUV emissions trace a slightly warped disc brighter in the North than in the South of the NIR photometric centre. The UV surface brightness profiles are flat in the inner ~ 60 arcsec and fall exponentially outward. There is no $H\alpha$ emission over the stellar disc in the z -direction, but the $H\alpha$ and UV discs are more extended radially than the old stellar population disc. The maximum emissions of NIR , $H\alpha$, NUV , and FUV agree within a ~ 5 arcsec at the centre of the galaxy. Jones et al. (2018) classified CIG 171 as not isolated using $H\text{ I}$ emission data.

CIG 183 (UGC 3791). Figure E4: The $H\alpha$ emission displays an asymmetric disc displaced to the Northeast outwards of the old stellar population disc. It also shows two big bright regions located at the North of the photometric centre and several remnant clouds that draw two tails in both sides of the $H\alpha$ disc. The $2.22\mu\text{m}$ emission shows a mostly symmetrical disc with a bulge and two plumes at the ends of the galactic major axis. The NUV and FUV emissions agree with the structure of the $H\alpha$ monochromatic map. The maxima of the NUV , FUV and $2.22\mu\text{m}$ emissions match within a circle of ~ 5 arcsec radius in the galactic centre. No additional spectral or photometric data are available yet in the literature to allow a conclusion about the morphology of this galaxy.

CIG 201 (UGC 3979). Figure E5: The $H\alpha$ emission map reveals a concentrated distribution of ionized gas, forming bright knots

predominantly located in the central region of the galaxy. A filamentary structure displayed by the ionized gas is consistently observed across all wavelengths. The K_s -band image shows a small disc that is symmetric but outwardly warped, tracing a similar shape to the $H\alpha$ and UV emission. The NUV , FUV , and $H\alpha$ maps display extended discs that exceed more than twice the area occupied by the NIR emission. The location of the $H\alpha$ bright knots match with the brightest knots seen in NUV and FUV emissions. The plateau shape of the NUV and FUV surface brightness profiles in the inner ~ 40 arcsec may be due to the emission of these bright regions uniformly distributed within a specified area. All the maps of CIG 201, presented in Figure E5, outline the same filamentary structure and display a cone shape at the galactic centre pointing Eastwards reaching different heights above the stellar disc. From SDSS data, Buta et al. (2019) classified CIG 201 as a SAc galaxy and identified an inner pseudoring (see Table 1). In addition, from $H\text{ I}$ emission data, Jones et al. (2018) determined that this galaxy is not interacting. The multi-wavelength morphology of CIG 201 suggests that the galactic disc may host a galactic wind.

CIG 329 (UGC 5010). Figure E6: The $H\alpha$ emission is distributed in a nearly symmetric ring structure. Indeed, Buta et al. (2019) classified it as a SAb galaxy identifying an inner pseudoring (see Table 1). The $2.22\mu\text{m}$ emission displays a long and symmetric disc with a central bulge and dust lane, with filaments along the edge. Following the photometric analysis of the K_s -band image, this galaxy has a ‘boxy’ bulge ($B_4 < 0$). The brightest FUV emission regions agree with the $H\alpha$ emission, while the faintest ones draw a filamentary warped disc and few detached clouds in the North. The NUV emission reveals a central dense distribution of the young stellar population, the NUV brightest clouds are consistent with the $2.22\mu\text{m}$ emission and the faintest draw filaments along the disc and the Northern cloud traced by the FUV emission. Based on the SDSS spectroscopy, Sabater et al. (2012) classified CIG 329 as a LINER. CIG 329 satisfies all the AMIGA sample isolation criteria (see Section 2).

CIG 416 (UGC 5642). Figure E7: The $H\alpha$ emission map displays an asymmetric filamentary wide and radially extended disc with a tail-shape at the Western tip and a few detached ionized gas clouds. The K_s -band image of this galaxy shows a small disc dominated by a bright central bulge. Beyond the K_s -band isophotal perimeter of the 3σ level, the old stellar population disc is asymmetric with a filamentary structure and a tail shape pointing Northwards at the West extreme. The phenomenon triggering the Western tail could be the reason for the non-linear relationship the B_4 parameter and the radius, however, neither the graphics nor the K_s -band image show the presence of a bar. The NUV and FUV images show even more extended asymmetric discs and larger detached clouds than the $H\alpha$ emission image. The images of these three bands present bright knots inside the disc. The photometric centre of the $H\alpha$, NIR , NUV and FUV emissions match quite well. The asymmetric disc is also observed at the optical wavelength since Buta et al. (2019) classified CIG 416 as Sdm peculiar using SDSS data. CIG 416 meets the isolation criteria of AMIGA sample in the optical band, nonetheless, it does not accomplish these criteria using radio band data (Jones et al. 2018). Therefore, the asymmetries, removed clouds, filaments and tails may be a signature of a past interaction.

CIG 593 (UGC 8598). Figure E8: Despite of a long exposure of 223 minutes (~ 4 hours), we only detected a few faint $H\alpha$ clouds tracing an asymmetric and truncated ionized gas distribution only visible on the North side, slightly displaced with respect to the major axis

of the old stellar population. It looks an ‘integral sign arm’ starting from a small bar. Indeed, [Buta et al. \(2019\)](#) classified this galaxy as a strongly barred (SB, see Table 1). The stellar disc shows a central bright bulge. The most diffuse *NIR* emission displays an asymmetric and truncated disc. The extended *NUV* emission disc covers the entire galaxy and draws a warped disc as the one traced by the *NIR* emission. The *FUV* emission brightest knots at the North are located in the same position as the $H\alpha$ clouds. The maxima of the *NUV*, *FUV* and *NIR* emissions are displaced by ~ 10 arcsec in the galactic centre. CIG 593 meets all the AMIGA sample isolation criteria (see Section 2).

CIG 847 (UGC 11132). Figure E9: The $H\alpha$ emission depicts a radially extended asymmetric and warped disc more prominent and brighter towards the South than to the North along the major axis with the maximum located towards the Southeast from the *NIR* photometric centre. The galaxy has a ionized gas tail-shape at the Southern tip and a detached cloud at the Northern edge. The $2.22\mu\text{m}$ emission reveals an almost symmetric elongated disc with small warp. The *FUV* emission only shows large disengaged clouds along the major axis instead of a dense disc giving as a result an inaccurate surface brightness profile. The *NUV* emission traces a long and warped disc with feathering along the borders of the disc, populating mainly the Northwest and with the maximum immediately to the North of the *NIR* photometric centre. Both $H\alpha$ and *NUV* emissions trace a tail shape at the Southeastern tip. The maxima of the *NUV* and *NIR* emissions match within ~ 5 arcsec in the galactic centre, while the *FUV* and $H\alpha$ emission maxima are located ~ 10 arcsec and ~ 15 arcsec Southwards from them, respectively. Using the $H\text{I}$ image of CIG 847, [Jones et al. \(2018\)](#) found that this galaxy fulfils the most strict isolation criteria of AMIGA sample (see Section 2).

CIG 906 (UGC 11723). Figure E10: After an exposure of 186 minutes (~ 3 hours) with FP GHASP, only faint $H\alpha$ clouds as knots were detected along the galactic major axis. A faint ionized gas cloud is located over the Northern edge of the stellar disc. The K_s -band image shows an old stellar population disc elongated and symmetrical with some filaments along the disc and a plume at the Southwest edge and a well-defined dust lane. The *NUV* and *FUV* emission display wider and brighter discs than the *NIR* one, both show filaments all along the edges of the disc and even some detached clouds. The surface brightness profiles of *NUV* and *FUV* emission show a discontinuity between the ellipses fitted to the 1σ and 3σ brightness levels of the K_s -band image, this is from ~ 30 and 45 arcsec. The maxima of the $H\alpha$, *NUV* and *FUV* emissions are displaced $\sim 10''$ Southwards from the *NIR* one. Despite [Buta et al. \(2019\)](#) classified CIG 906 as Sbc, our analysis to the surface brightness profile of the $2.2\mu\text{m}$ image showed a ‘disc-like’ shape. According with [Jones et al. \(2018\)](#), from $H\text{I}$ data, CIG 906 is a well isolated galaxy.

CIG 922 (UGC 11785). Figure E11: The $H\alpha$ emission disc is asymmetric and warped, it dominates the Northern galactic region and it is composed by large detached clouds. The ionized gas disc is wider and longer than the old stellar disc. The $H\alpha$ cloud furthest North is faint and exceeds radially the old stellar disc tracing an arrow-shape, while to the South there are two $H\alpha$ detached bright knots just outside of the *NIR* disc edge. The old stellar population disc is mostly symmetric and elongated, it has a central bulge. The faintest *NIR* emission shows a warp at the Northeastern and a plume outside the Southwestern tip of the stellar disc, both peculiarities are pointing to the Southeast. The *FUV* emission traces a wider and

denser disc than the $H\alpha$ emission disc but both match in shape: the rounded Southern tip and the Northern arrow-shaped. The *NUV* emission displays the most extended disc, with large plumes at one side of the disc pointing to the Northwest, and a detached cloud at the Northern tip. The maxima of the four emissions matches within the central ~ 5 arcsec. [Buta et al. \(2019\)](#) classified CIG 922 as Scd warped galaxy (see Table 1) and, from $H\text{I}$ data, [Jones et al. \(2018\)](#) determined that this galaxy is not strictly isolated: the morphology of CIG 922 might be a result of some interaction.

CIG 936 (UGC 11859). Figure E12: The K_s -band and most of $H\alpha$ emissions were detected in the central 30 arcsec of a galaxy with an optical diameter of $D_{25}(B) = 185.4$ arcsec (see Table 1 and Figure E12a). The $H\alpha$ monochromatic image shows most of the warm gas compressed at the centre within the old stellar population disc, drawing a cone-shape. The K_s -band image shows an asymmetric disc with a central bulge. The *FUV* emission draws an extended thin disc (isophotal radius $r_{FUV} = 47.6$ arcsec, see Table 5) whose tips are warped pointing to the Northwest. The *NUV* disc emission is wider than the *FUV* one, with filaments mainly along the Southeastern side of the disc with the largest and broadest filament at the galactic centre. At ~ 70 arcsec Southwards from the galactic centre, there is a *NUV* bright knot on the disc matching with the DSS R-band image and a faint $H\alpha$ cloud, which is probably a SF region because it is not detected at the *NIR* emission. The maxima of the four emissions matches in the galactic centre. [Jones et al. \(2018\)](#) classified this galaxy as $H\text{I}$ -not-isolated (see Section 2).

CIG 1003 (UGC 12304). Figure E13: The ionized gas is compressed in the central region of the disc which presents three bright knots, one at the centre and the other two symmetrically placed ~ 15 arcsec away. The $H\alpha$ emission map displays filaments of ionized gas in all the edges, but the most prominent of them are around the central knot tracing a cone-shape pointing to the Southwest. The K_s -band image shows an elongated and symmetric stellar disc with a central bulge. The diffuse *NIR* emission displays a cone-shape at the galactic centre pointing Southwest and a hook-shaped extension at the Northern tip pointing Northeast. The *NUV* emission image shows a prominent filament of ~ 15 arcsec length pointing to the Southwest; in addition, the cone-shape in the central region is more noticeable in this emission. The *FUV* and *NUV* emission maps reveal very extended asymmetric and warped discs. Also, the brightest knots in these bands, match the Southern $H\alpha$ knot. All the photometric centres defined by the ellipse fitting lay on the central $H\alpha$ knot agreeing within ~ 5 arcsec. CIG 1003 displays thinner discs Northwards and wider Southwards in the *NIR*, *FUV*, and *NUV* emissions. CIG 1003’s multiwavelength morphology, position on the region of bona fide isolated galaxies (see Figure 2) and $H\text{I}$ classification as not isolated ([Jones et al. 2018](#)), suggest that it has a galactic wind, possibly due to a recent interaction.

APPENDIX E: INDIVIDUAL MAPS

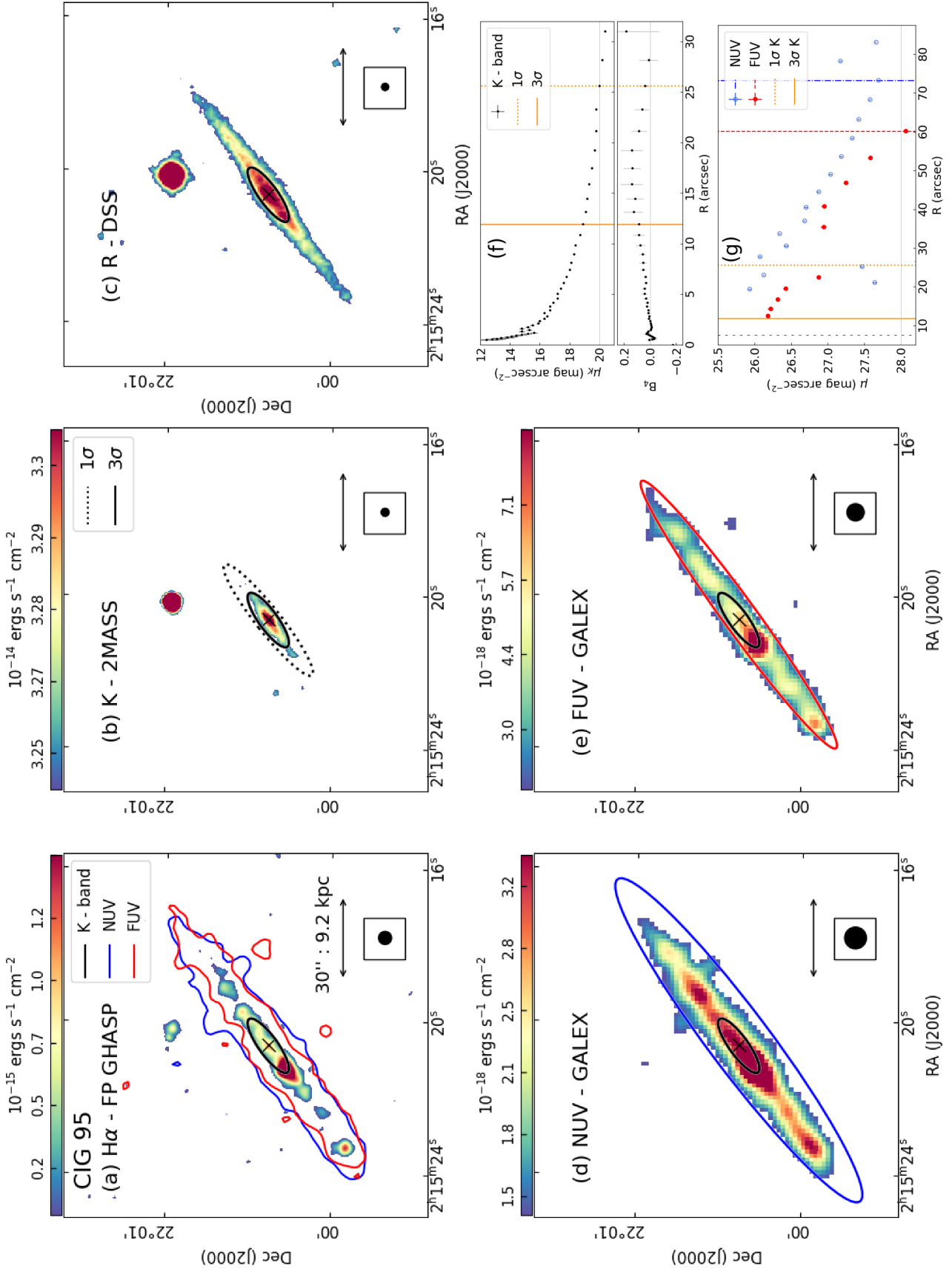


Figure E1. CIG95 (UGC 1733). Same as Figure 3.

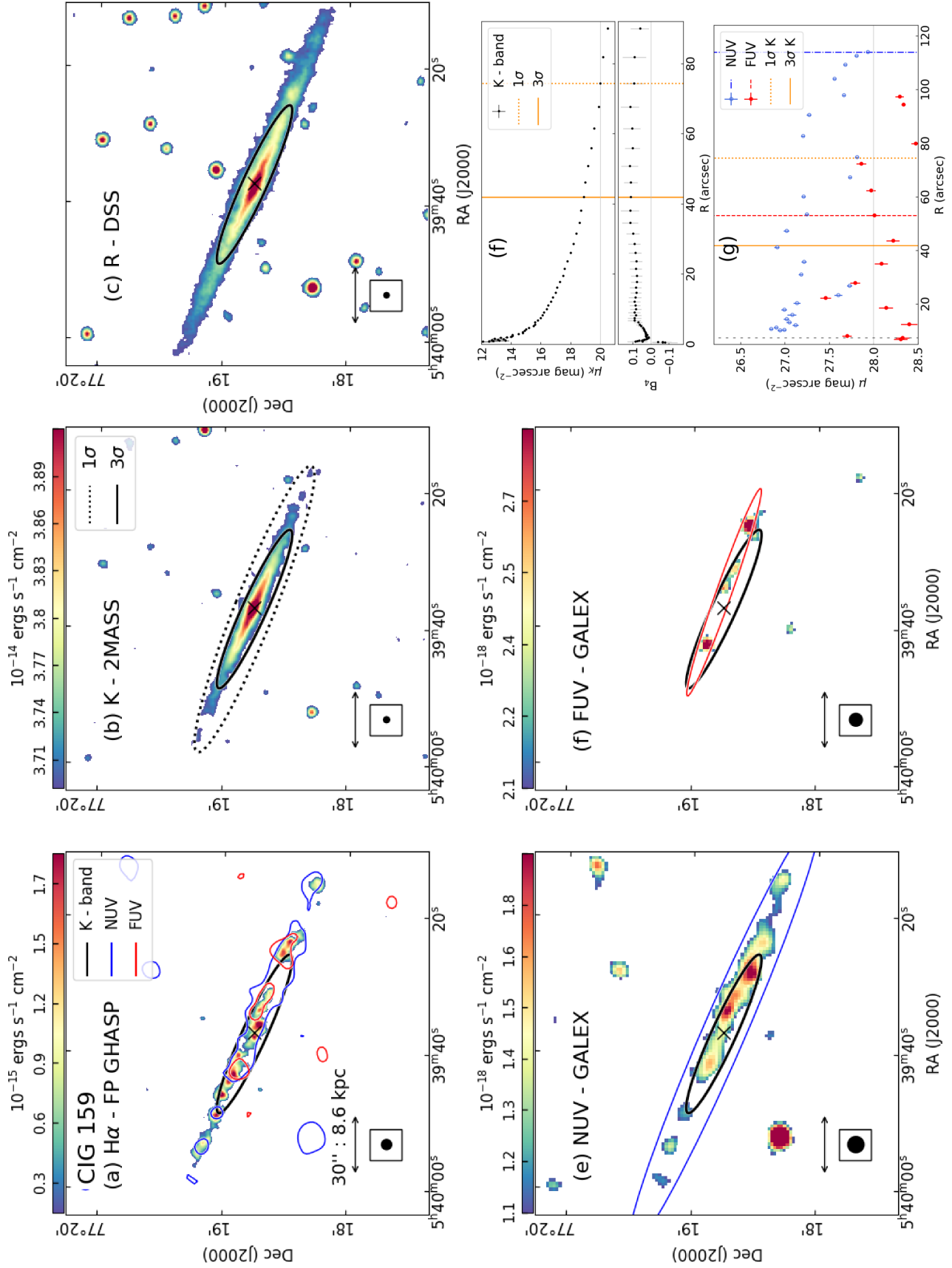


Figure E2. CIG 159 (UGC 3326). Same as Figure 3.

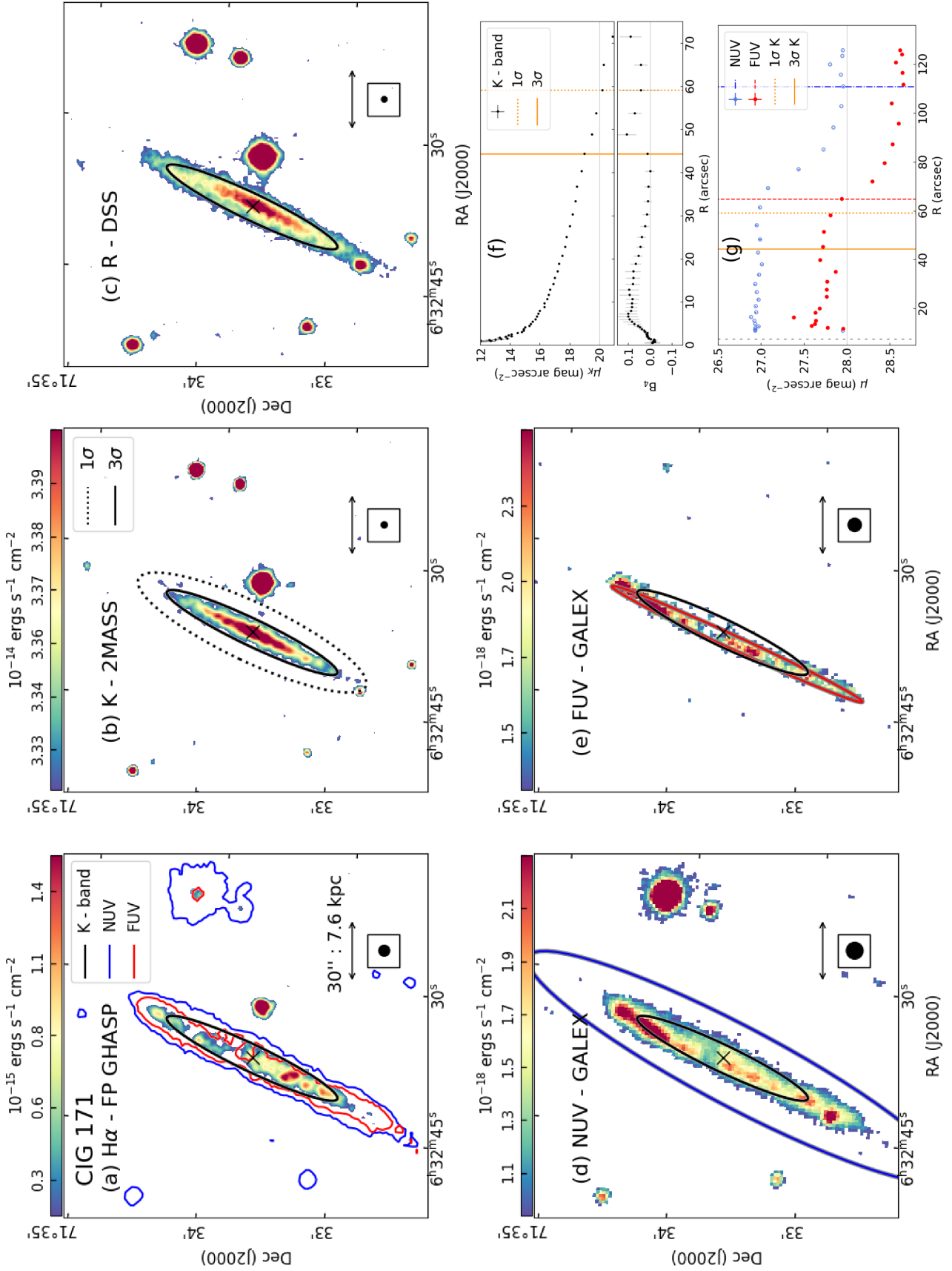


Figure E3. CIG 171 (UGC 3474). Same as Figure 3.

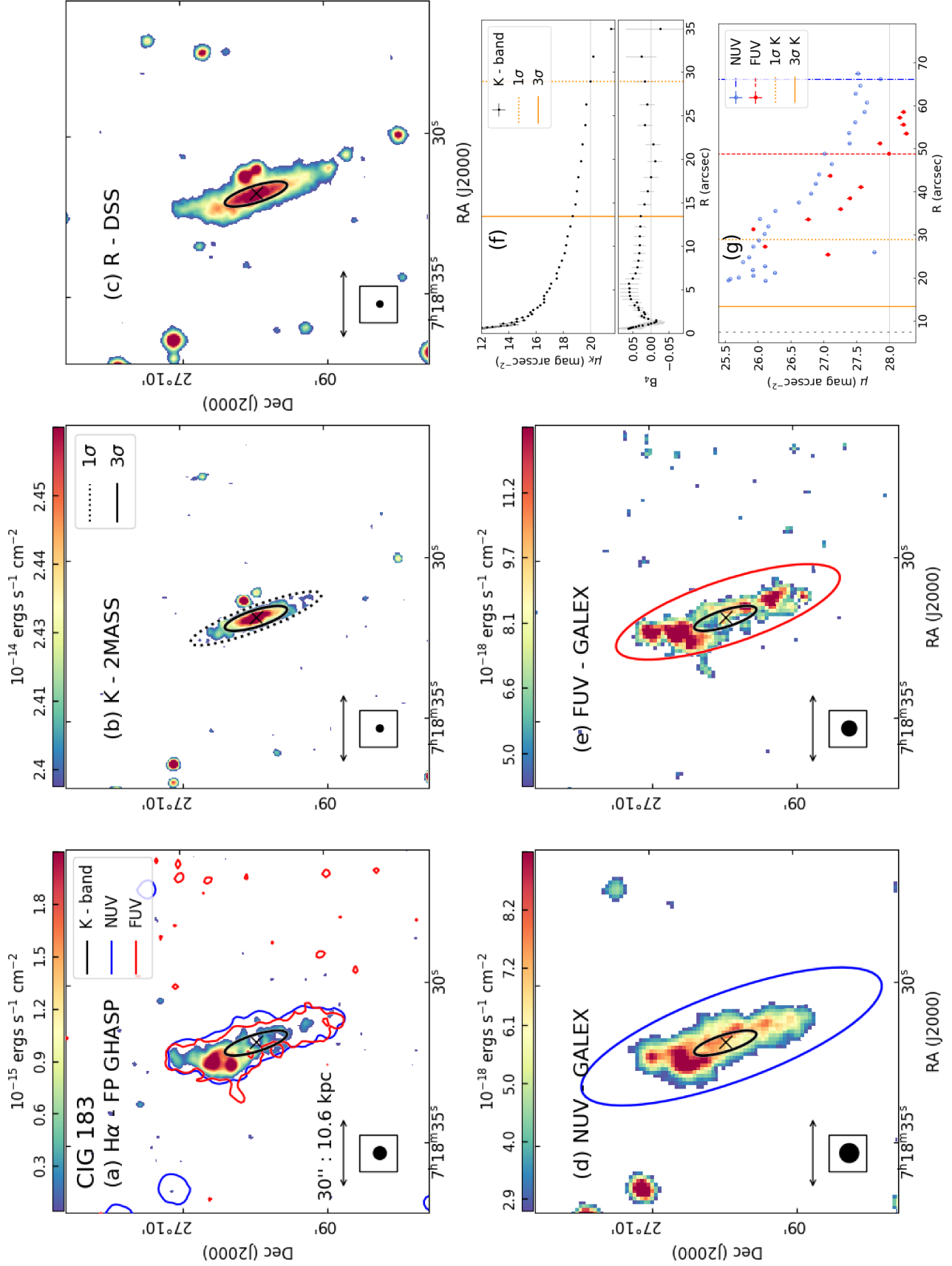


Figure E4. CIG 183 (UGC 3791). Same as Figure 3.

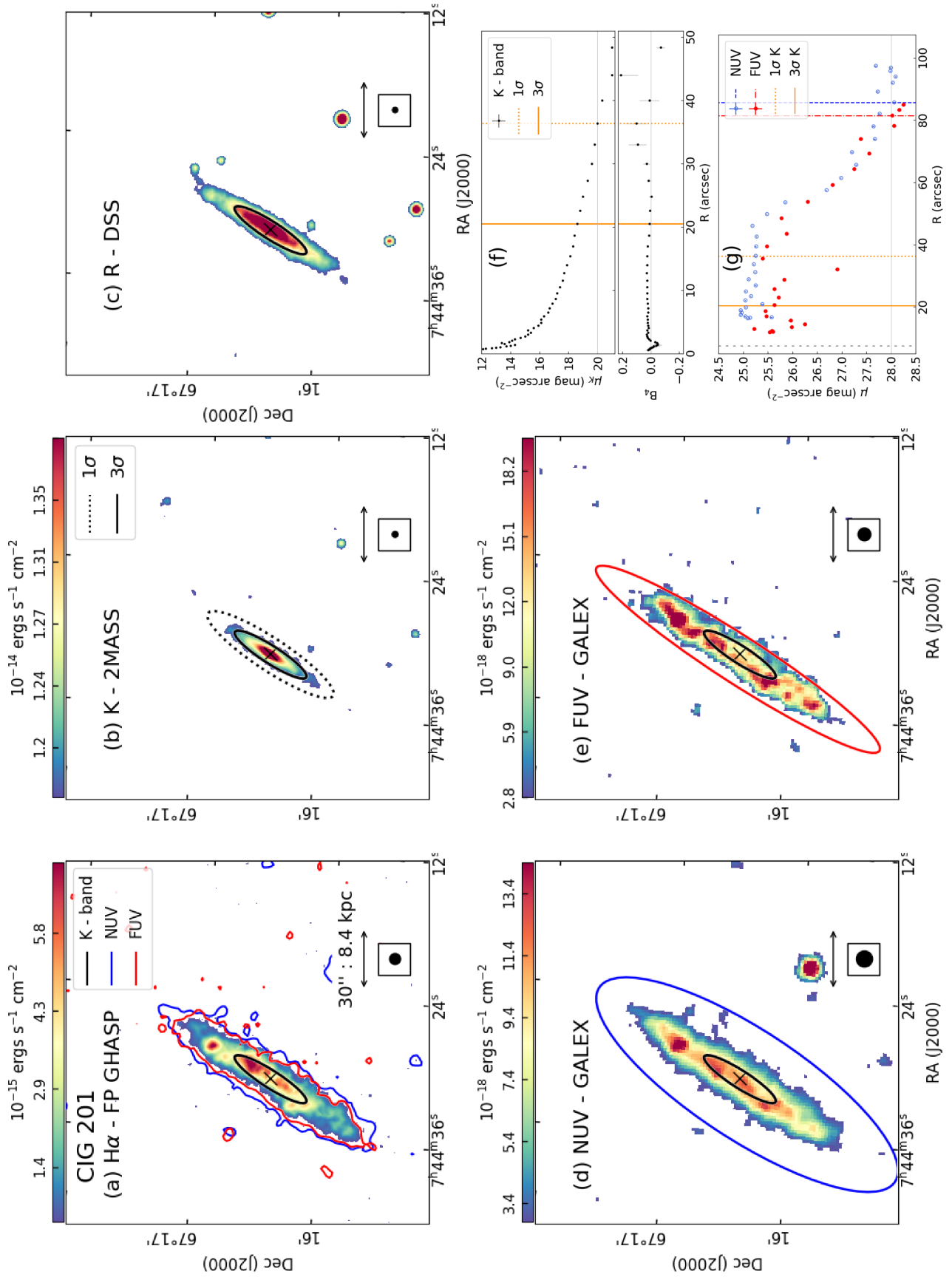


Figure E5. CIG 201 (UGC 3979). Same as Figure 3.

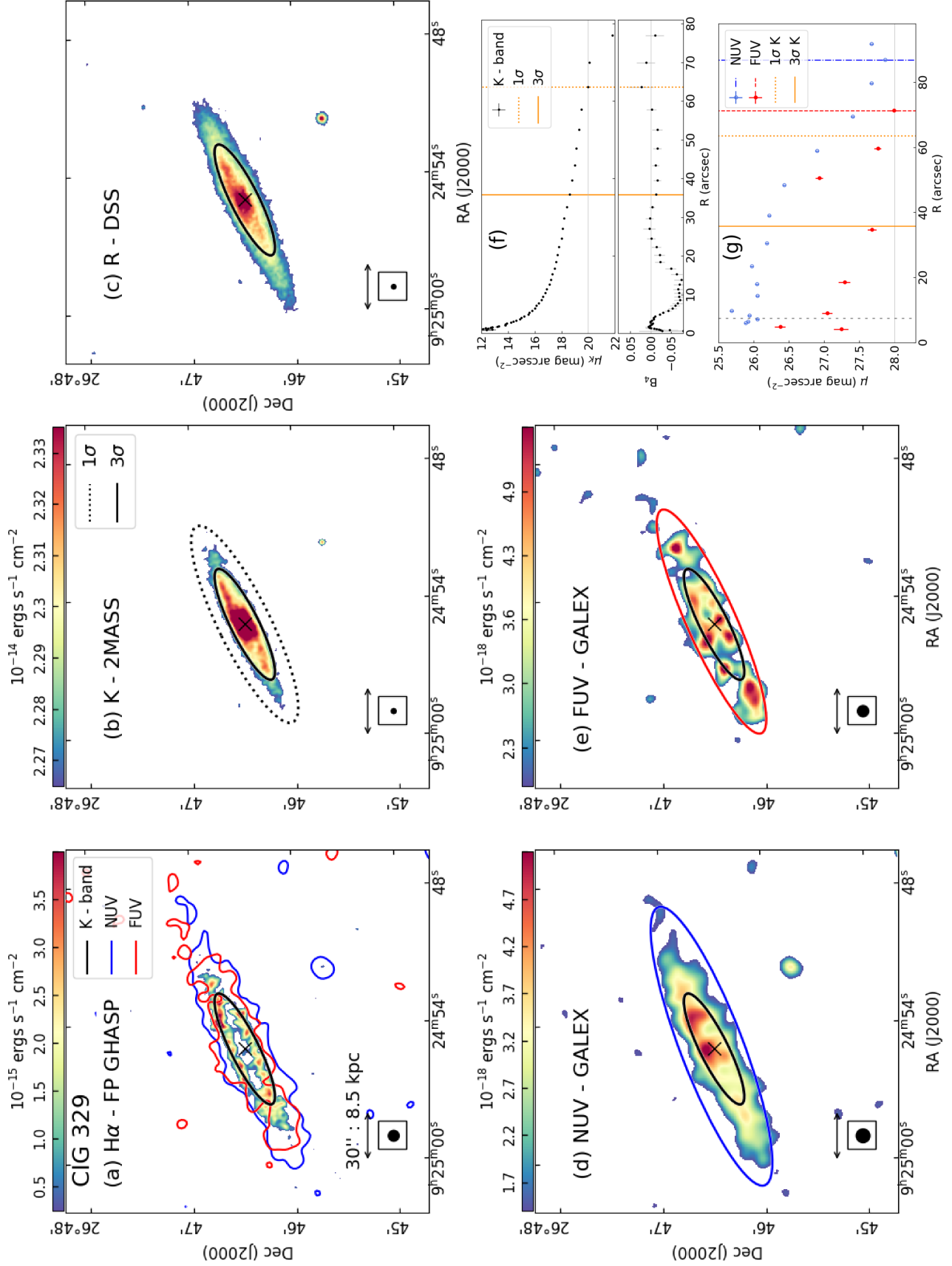


Figure E6. CIG 329 (UGC 5010). Same as Figure 3.

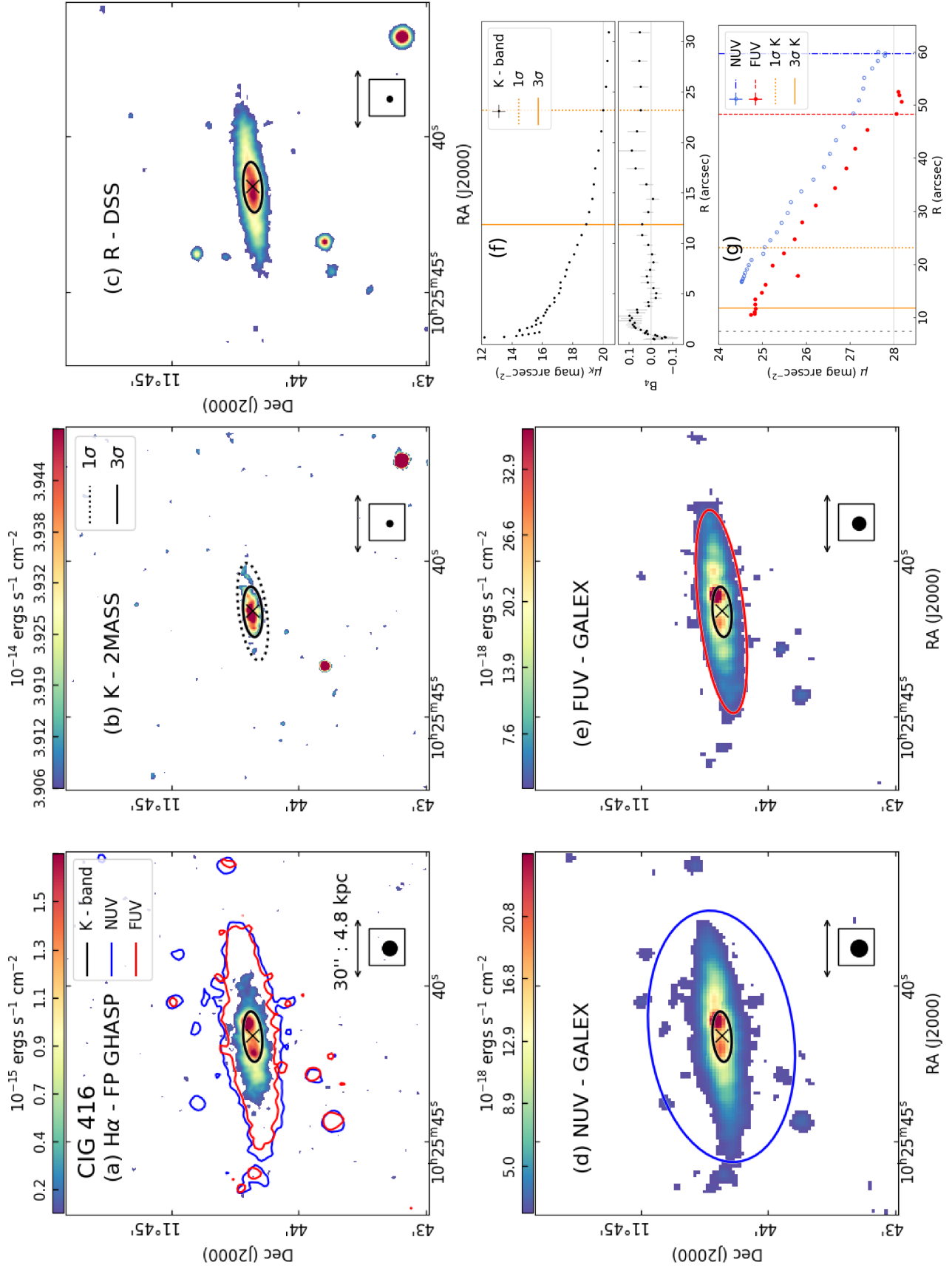


Figure E7. CIG 416 (UGC 5642). Same as Figure 3.

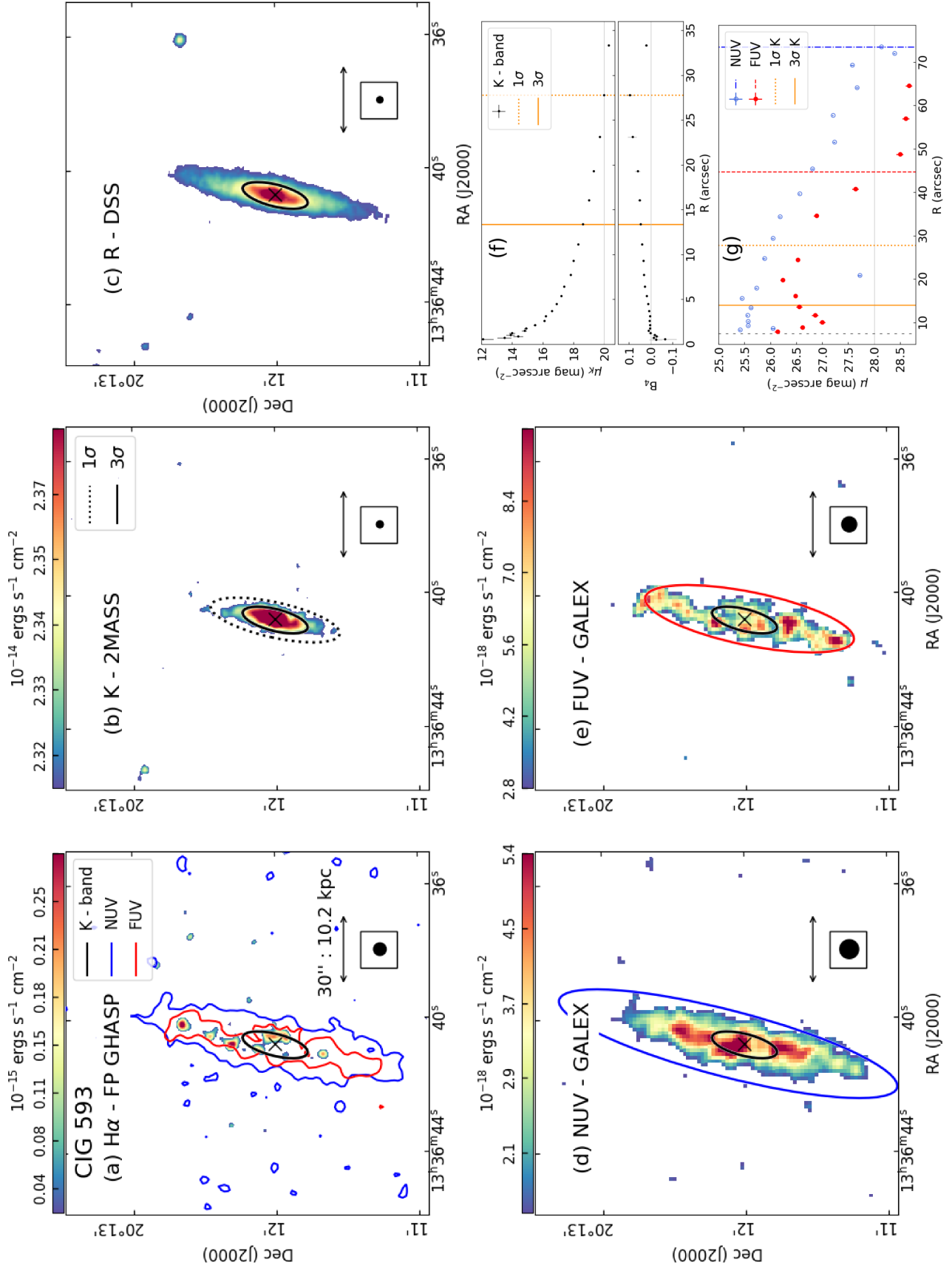


Figure E8. CIG 593 (UGC 8598). Same as Figure 3.

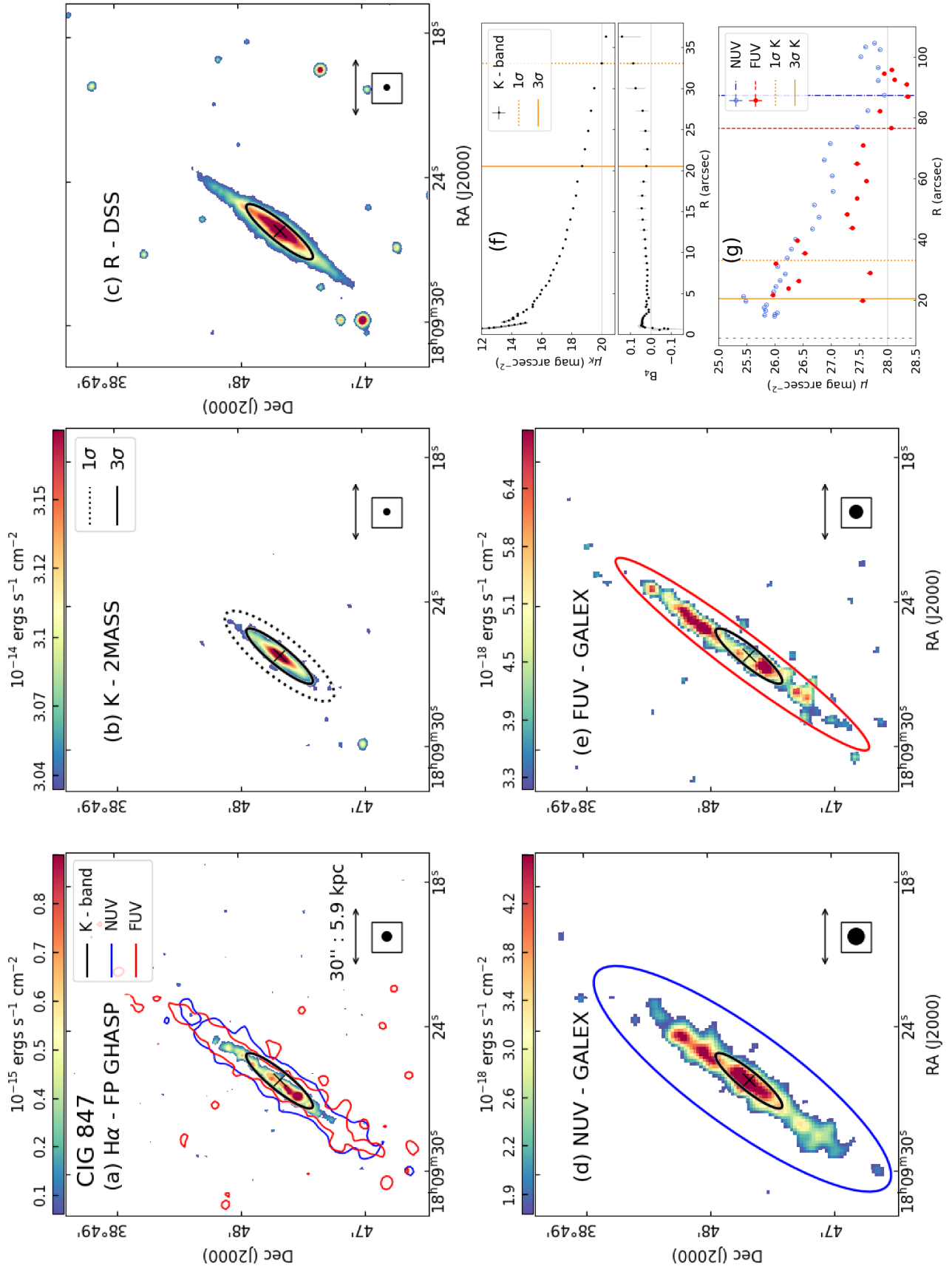


Figure E9, CIG 847 (UGC 11132). Same as Figure 3.

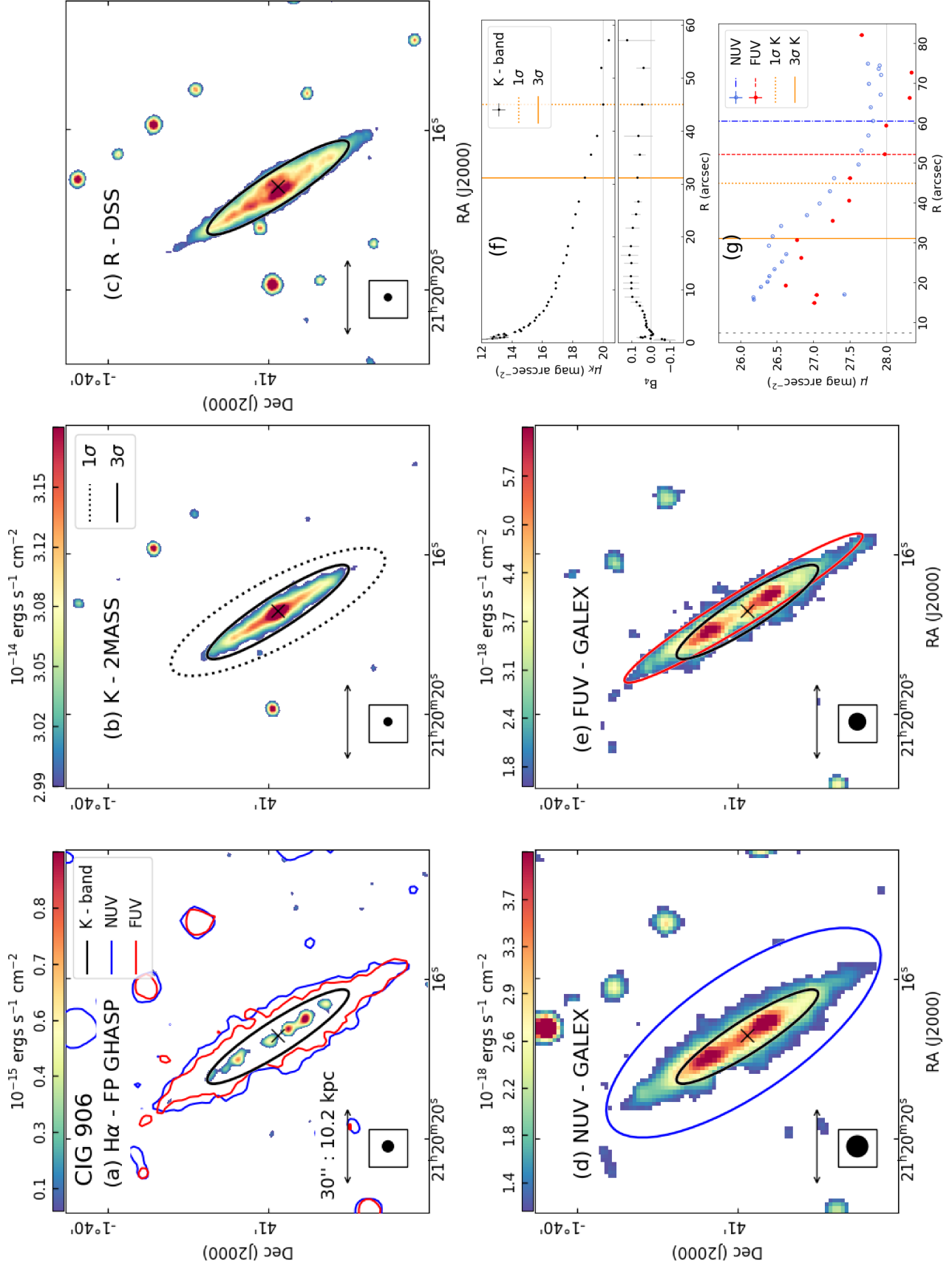


Figure E10. CIG 906 (UGC 11723). Same as Figure 3.

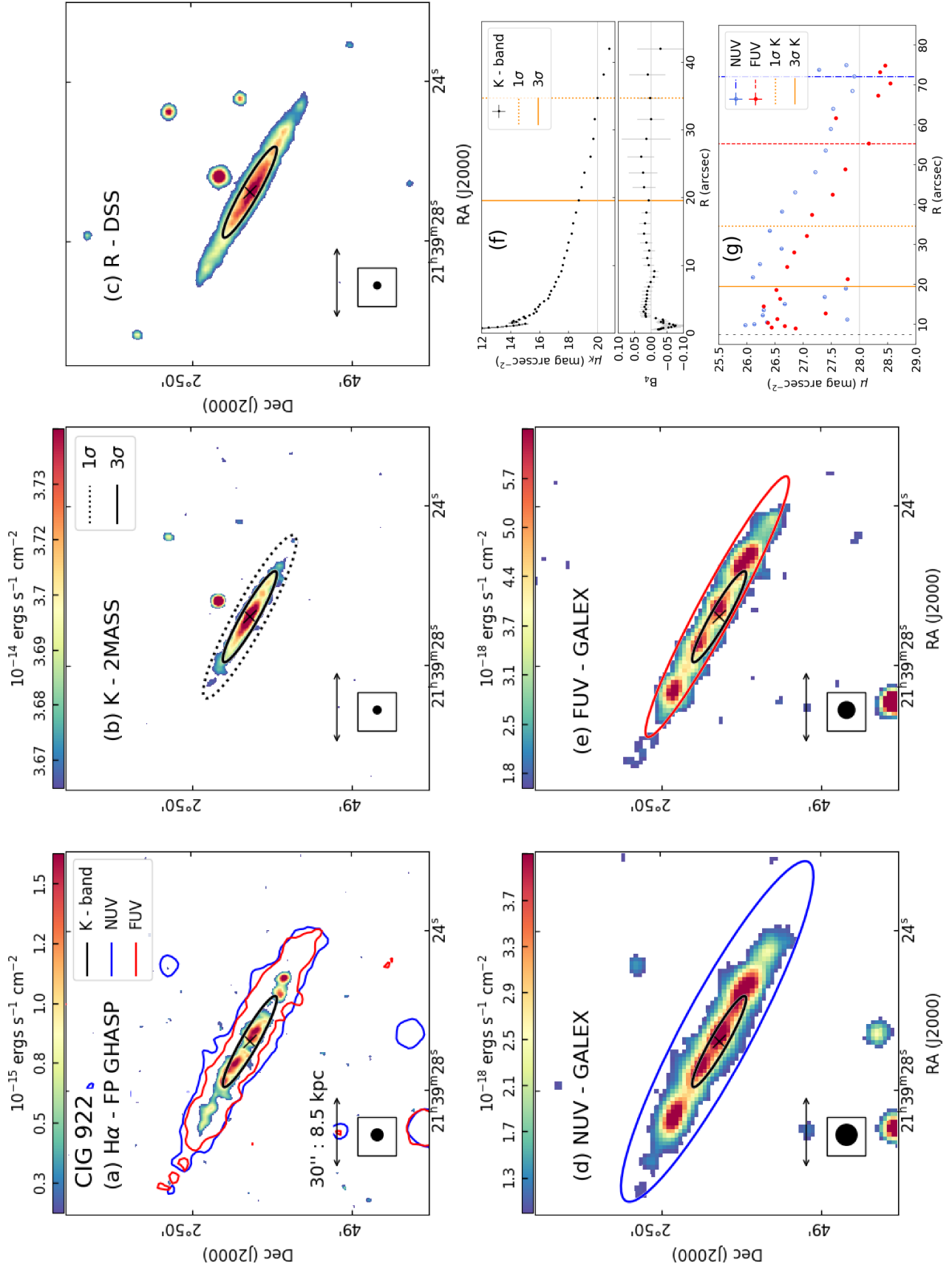


Figure E11. CIG 922 (UGC 11785). Same as Figure 3.

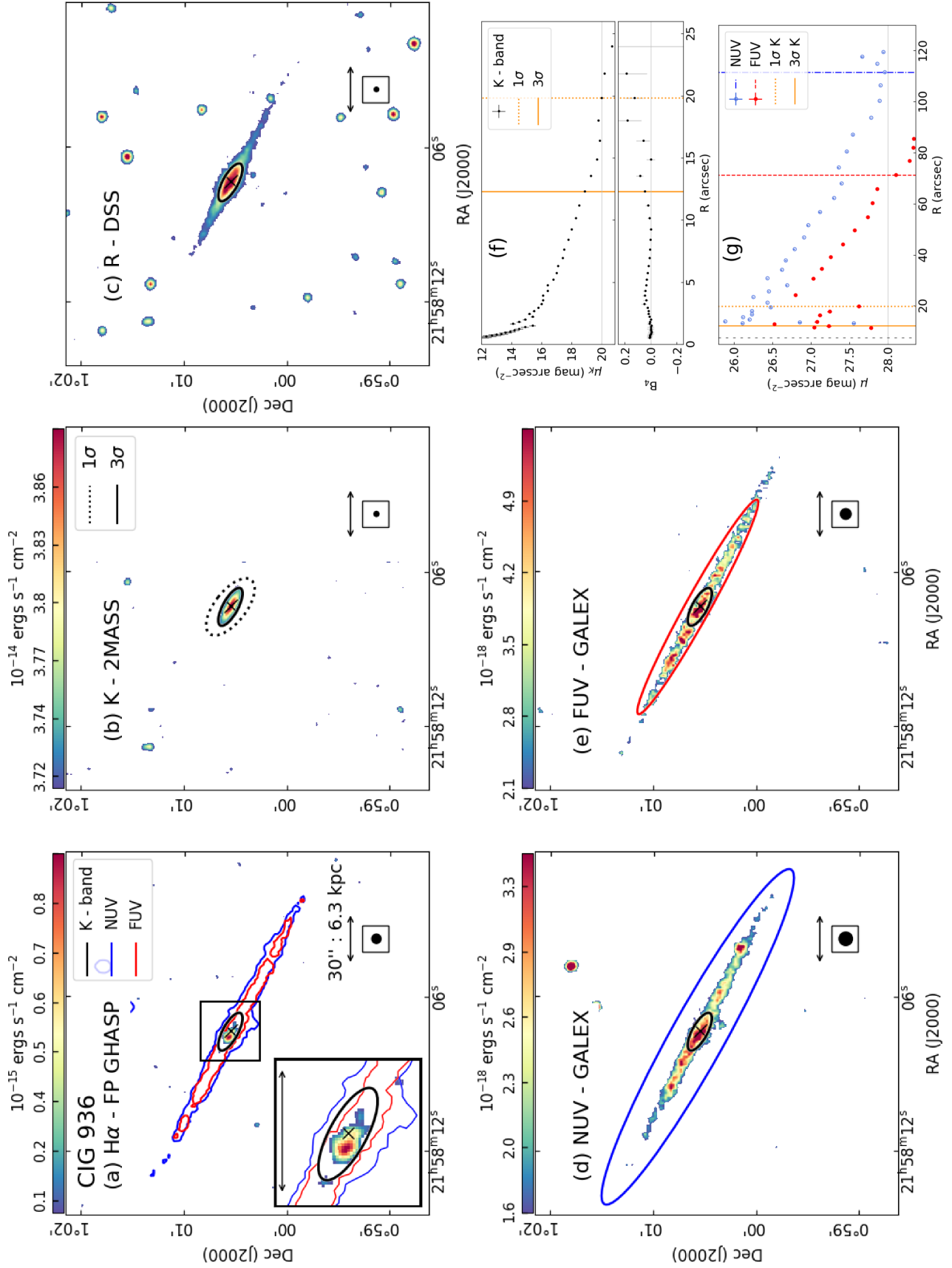


Figure E12. CIG 936 (UGC 11859). Same as Figure 3.

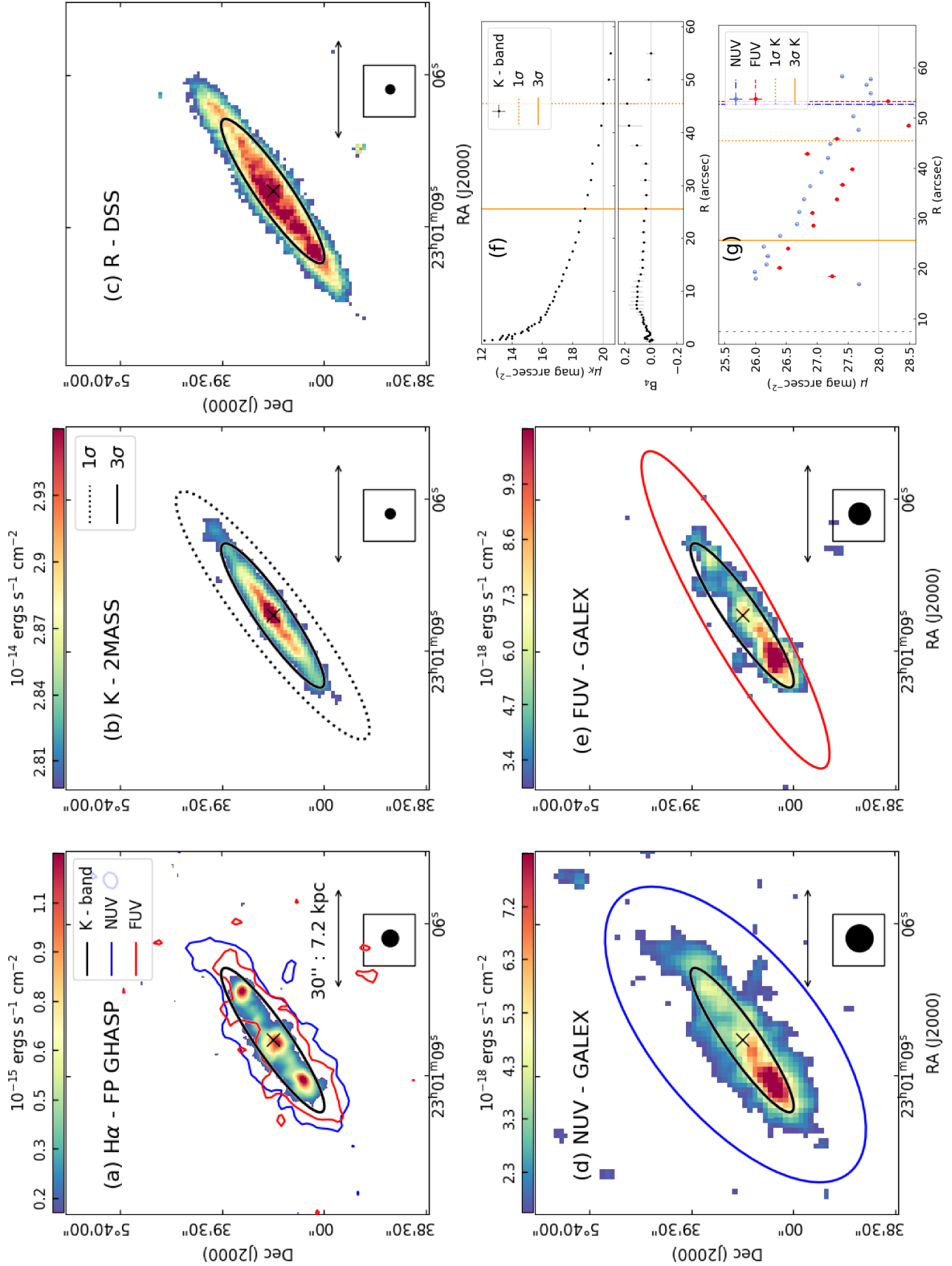


Figure E13. CIG 1003 (UGC 12304). Same as Figure 3.

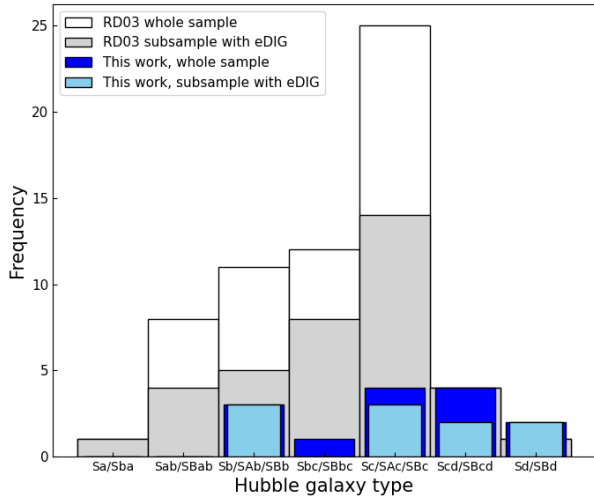


Figure F1. Histogram of the Hubble galaxy type distribution of the whole galaxy sample of [Rossa & Dettmar \(2003a\)](#) (RD03) (see Table F1) and their subsample of galaxies presenting eDIG compared with the Hubble galaxy type of our galaxy sample and our subsample of galaxies presenting eDIG.

APPENDIX F: ROSSA & DETTMAR (2003A) SAMPLE

Table F1: The sample of [Rossa & Dettmar \(2003a\)](#).

Object Name	RA J2000.0	Dec J2000.0	Hubble type	V_{sys} km s ⁻¹	Log ₁₀ M _* (M _⊙)	L_{FIR}/D_{25}^2 (10 ⁴⁰ ergs s ⁻¹ kpc ⁻²)	S ₆₀ /S ₁₀₀	eDIG	Interact	Ref.
(1)	(2)	(3)	(4)	(5)	(6)	(7)	(8)	(9)	(10)	(11)
NGC 24	00h09m56.54s	-24d57m47.3s	Sc	554	8.0	0.77	0.3396		p	(i)
NGC 100	00h24m02.84s	+16d29m11.0s	Sc	844	8.3	0.21	0.1971		i	(i)
UGC 260	00h27m02.92s	+11d35m01.7s	Sc	2134	9.8	3.30	0.3761	*	p	(i)
ESO 540–16	00h42m14.69s	-18d09m42.5s	SBcd	1559	10.0	0.64	0.3692	*	i	(ii)
NGC 360	01h02m51.45s	-65d36m35.9s	Sc	2306	8.9	1.94	0.1609	*	i	(iii)
NGC 669	01h47m16.15s	+35d33m47.9s	Sab	4674	8.0	1.04	0.2455		g	(i)
NGC 891	02h22m33.41s	+42d20m56.9s	Sb	528	5.9	3.19	0.2089	*	g	(i)
UGC 2082	02h36m16.15s	+25d25m25.8s	Sc	708	5.5	0.35	0.2356		i	(i)
IC 1862	02h51m58.80s	-33d20m24.6s	Sbc	6395	7.0	2.48	0.3357		g	(i)
NGC 1247	03h12m14.32s	-10d28m52.0s	Sab	3947	8.8	2.92	0.3604	*	g	(i)
ESO 117–19	04h02m32.13s	-62d18m56.2s	SBbc	5335	6.2	3.51	0.2759	*	g	(ii)
IC 2058	04h17m54.35s	-55d55m58.4s	Sc	1379	5.1	1.15	0.2982		p	(i)
ESO 362–11	05h16m38.80s	-37d06m09.1s	Sbc	1345	7.6	2.63	0.3295	*	g	(ii)
IC 2135	05h33m12.90s	-36d23m55.8s	Sc*	1312	7.3	7.28	0.4051	*	i	(ii)
ESO 121–6	06h07m29.85s	-61d48m27.3s	Sc	1203	10.2	7.05	0.3256	*	i	(ii)
NGC 2188	06h10m09.53s	-34d06m22.3s	SBcd	747	8.4	1.63	0.4301	*	i	(iii)
ESO 209–9	07h58m15.01s	-49d51m05.1s	SBC	1126	9.1	4.56	0.2948	*	i	(ii)
UGC 4559	08h44m07.61s	+30d07m08.9s	Sb	2085	7.8	0.89	0.2721		i	(iii)
NGC 2654	08h49m11.87s	+60d13m16.0s	SBab	1339	7.3	0.57	0.1882		i	(i)
NGC 2683	08h52m41.33s	+33d25m18.3s	Sb	411	3.7	1.76	0.1976		i	(i)
NGC 3003	09h48m36.05s	+33d25m17.4s	SBC	1480	6.7	1.65	0.3434		g	(i)
NGC 3044	09h53m40.88s	+01d34m46.7s	Sbc*	1289	9.9	6.72	0.4633	*	g	(i)
NGC 3221	10h22m19.98s	+21d34m10.5s	SBcd	4111	10.5	13.80	0.3738	*	i	(iii)
NGC 3600	11h15m52.01s	+41d35m27.7s	Sab	703	9.3	1.30	0.4362	*	i	(i)
NGC 3628	11h20m16.97s	+13d35m22.9s	Sb	846	8.9	5.02	0.4694	*	g	(i)
NGC 3877	11h46m07.70s	+47d29m39.6s	Sc	895	6.8	4.15	0.2486	*	g	(i)
NGC 3936	11h52m20.59s	-26d54m21.2s	SBbc	2013	9.4	2.03	0.2447		g	(i)
ESO 379–6	11h53m03.27s	-36d38m19.8s	Sbc	2944	8.8	3.67	0.2452	*	i	(ii)
NGC 4206	12h15m16.81s	+13d01m26.3s	Sc	703	10.7	0.53	0.2054	*	g	(i)
NGC 4216	12h15m54.44s	+13d08m57.8s	SBab	131	10.6	0.59	0.1221		g	(i)
NGC 4235	12h17m09.88s	+07d11m29.7s	Sa	2263	8.7	0.37	0.4896	*	g	(i)
NGC 4256	12h18m43.09s	+65d53m53.7s	Sb	2489	4.6	0.71	0.1794		g	(i)
NGC 4302	12h21m42.48s	+14d35m53.9s	Sc*	1098	8.5	3.69	0.2136	*	p	(i)
NGC 4388	12h25m46.75s	+12d39m43.5s	Sb	2524	10.5	5.53	0.6127	*	g	(i)
NGC 4402	12h26m07.65s	+13d06m48.0s	Sb*	237	7.0	7.82	0.3320	*	g	(i)
NGC 4634	12h42m40.96s	+14d17m45.0s	Sbc*	139	5.0	11.84	0.3720	*	p	(i)
NGC 4700	12h49m08.15s	-11d24m35.5s	SBC	1409	8.3	4.99	0.5074	*	g	(i)
NGC 4945	13h05m27.48s	-49d28m05.6s	SBC	563	4.8	14.79	0.5661	*	g	(i)
NGC 5170	13h29m48.79s	-17d57m59.1s	Sc*	1501	8.8	0.34	0.2796		g	(i)
NGC 5290	13h45m19.18s	+41d42m45.3s	Sbc	2549	7.8	2.57	0.3139	*	g	(i)
NGC 5297	13h46m23.67s	+43d52m20.4s	SBbc	2409	7.2	1.69	0.2714		p	(i)
IC 4351	13h57m54.26s	-29d18m56.6s	Sb*	2674	7.9	1.48	0.1947		g	(i)
NGC 5775	14h53m57.60s	+03d32m40.0s	SBC	1676	6.4	21.49	0.3415	*	p	(i)
ESO 274–1	15h14m13.43s	-46d48m33.1s	Sd	524	8.6	0.19	0.5055	*	i	(ii)
NGC 5965	15h34m02.46s	+56d41m08.2s	Sb	3377	6.3	0.55	0.2769		p	(i)
UGC 10288	16h14m24.80s	-00d12m27.1s	SABc	2044	8.5	0.89	0.2370		g	(i)
IC 4837	19h15m14.64s	-54d39m41.1s	Sab	2668	8.3	2.42	0.2605	*	g	(i)
NGC 6875	20h13m12.47s	-46d09m41.9s	SBC	3121	9.0	1.56	0.3048	*	p	(i)
MCG-01-53-012	20h49m52.23s	-07d01m18.5s	Sc	6024	8.6	0.94	0.2067		i	(ii)
IC 5052	20h52m05.57s	-69d12m05.9s	SBcd	584	9.5	1.00	0.3112	*	g	(i)
IC 5071	21h01m19.74s	-72d38m33.8s	SABb	3123	8.0	1.41	0.2472	*	g	(i)
IC 5096	21h18m21.54s	-63d45m38.4s	Sbc	3144	7.4	1.42	0.2280		g	(i)
NGC 7064	21h29m02.98s	-52d46m03.4s	SBC	767	5.1	1.06	0.6250	*	g	(i)
NGC 7090	21h36m28.86s	-54d33m26.4s	SBC	847	4.6	1.95	0.3287	*	g	(i)
NGC 7184	22h02m39.82s	-20d48m46.2s	SBC	2623	9.6	1.38	0.2588		i	(iii)
IC 5171	22h10m56.70s	-46d04m53.3s	SBb	2847	7.8	1.86	0.3101	*	g	(ii)
IC 5176	22h14m55.93s	-66d50m57.9s	SBbc	1748	5.9	3.51	0.3044	*	g	(ii)
NGC 7361	22h42m17.91s	-30d03m27.6s	Sc*	1249	7.8	1.07	0.2669		i	(i)
UGC 12281	22h59m12.80s	+13d36m24.0s	Sc	2562	5.3	0.98	0.1830		g	(i)
NGC 7462	23h02m46.49s	-40d50m06.9s	SBbc	1064	10.0	3.34	0.4492	*	g	(i)
NGC 7640	23h22m06.58s	+40d50m43.5s	SBC	369	8.1	0.45	0.2259		g	(i)
ESO 240–11	23h37m49.42s	-47d43m38.4s	Sb	2836	5.9	1.00	0.1776		g	(ii)

Table F1: The sample of [Rossa & Dettmar \(2003a\)](#).

Object Name	RA	Dec	Hubble	V_{sys}	$\text{Log}_{10} M_*$	L_{FIR}/D_{25}^2	S_{60}/S_{100}	eDIG	Interact	Ref.
(1)	J2000.0	J2000.0	type	km s^{-1}	(M_{\odot})	($10^{40} \text{ ergs s}^{-1} \text{ kpc}^{-2}$)	(8)	(9)	(10)	(11)

Columns: (1) object name; (2) and (3) wcs coordinates (J2000);

(4) Hubble type from [Rossa & Dettmar \(2003b\)](#), when unavailable, marked by (*) from HyperLeda ([HyperLEDA 2016](#));

(5) heliocentric velocity (V_{sys}); (6) logarithm of the stellar mass computed with *MIR*-band photometry (see equation C1);

(7) and (8) DDD parameters from [Rossa & Dettmar \(2003a\)](#): *FIR* luminosity (L_{FIR}) divided by the optical diameter of the 25^{th} mag/arcsec isophote squared (D_{25}^2) and flux densities ratio at $60 \mu\text{m}$ and $100 \mu\text{m}$ (S_{60}/S_{100}), respectively;

(9) cases where the eDIG was detected by [Rossa & Dettmar \(2003a\)](#);

(10) hierarchy reported so far in the literature: i: isolated or no records, p: pair member, g: group member;

(11) hierarchy reference: (i) NED, (ii) SIMBAD, (iii) There is no record.

This paper has been typeset from a \TeX/L\AA\TeX file prepared by the author.